AD-A109 644 R AND D ASSOCIATES MARINA DEL REY CA F/G 18/3
SOME ANALYTIC MODELS FOR QUASI-STATIC SOURCE REGION EMP: APPLIC--ETC(U)
NOV 80 M K GROVER DNA001-80-C-0069
UNCLASSIFIED RDA-TR-113202-002 DNA-5800T NL

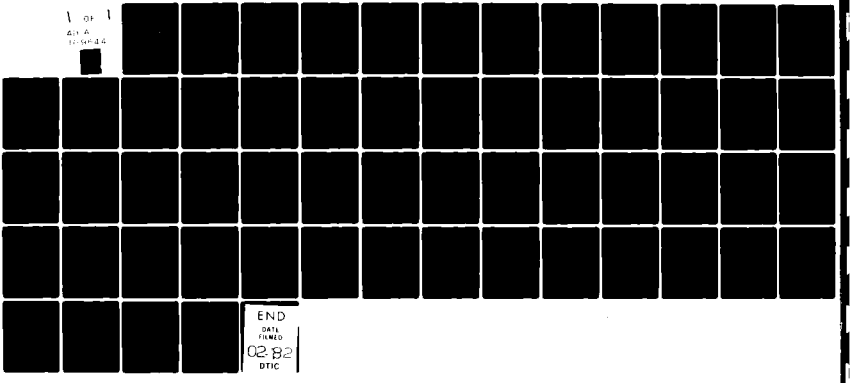

END
DATE FILMED
02 82
DTIC

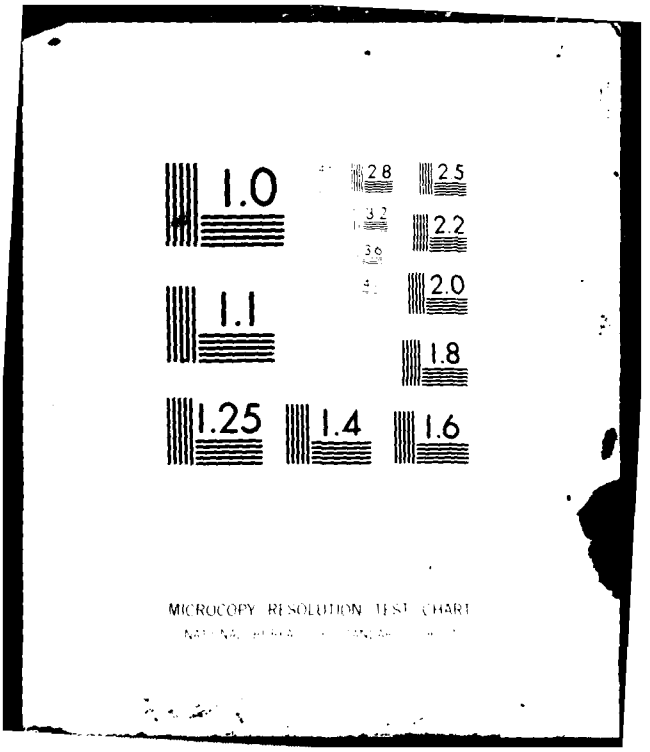
1.0
2.8
2.5
3.2
2.2
3.6
2.0
1.1
1.8
1.25
1.4
1.6
MICROCOPY RESOLUTION TEST CHART

(12)

DNA 5800T

SOME ANALYTIC MODELS FOR QUASI-STATIC SOURCE REGION EMP: APPLICATION TO NUCLEAR LIGHTNING

M. K. Grover
R&D Associates
P.O. Box 9695
Marina del Rey, California 90291

1 November 1980

Topical Report for Period 5 January 1980—1 November 1980

CONTRACT No. DNA 001-80-C-0069

APPROVED FOR PUBLIC RELEASE;
DISTRIBUTION UNLIMITED.

THIS WORK SPONSORED BY THE DEFENSE NUCLEAR AGENCY
UNDER RDT&E RMSS CODE B310080464 P99QAXDB00157 H2590D.

Prepared for
Director
DEFENSE NUCLEAR AGENCY
Washington, D. C. 20305

Destroy this report when it is no longer needed. Do not return to sender.

PLEASE NOTIFY THE DEFENSE NUCLEAR AGENCY, ATTN: STTI, WASHINGTON, D.C. 20305, IF YOUR ADDRESS IS INCORRECT, IF YOU WISH TO BE DELETED FROM THE DISTRIBUTION LIST, OR IF THE ADDRESSEE IS NO LONGER EMPLOYED BY YOUR ORGANIZATION.

UNCLASSIFIED

SECURITY CLASSIFICATION OF THIS PAGE *(When Data Entered)*

REPORT DOCUMENTATION PAGE		READ INSTRUCTIONS BEFORE COMPLETING FORM
1. REPORT NUMBER DNA 5800T	2. GOVT ACCESSION NO. AD-A109	3. RECIPIENT'S CATALOG NUMBER 644
4. TITLE *(and Subtitle)* SOME ANALYTIC MODELS FOR QUASI-STATIC SOURCE REGION EMP: APPLICATION TO NUCLEAR LIGHTNING		5. TYPE OF REPORT & PERIOD COVERED Topical Report for Period 5 Jan 80—1 Nov 80
		6. PERFORMING ORG. REPORT NUMBER RDA-TR-113202-002
7. AUTHOR(s) M. K. Grover		8. CONTRACT OR GRANT NUMBER(s) DNA 001-80-C-0069
9. PERFORMING ORGANIZATION NAME AND ADDRESS R & D Associates P.O. Box 9695 Marina del Rey, California 90291		10. PROGRAM ELEMENT, PROJECT, TASK AREA & WORK UNIT NUMBERS Subtask P99QAXDB001-57
11. CONTROLLING OFFICE NAME AND ADDRESS Director Defense Nuclear Agency Washington, D.C. 20305		12. REPORT DATE 1 November 1980 13. NUMBER OF PAGES 58
14. MONITORING AGENCY NAME & ADDRESS*(if different from Controlling Office)*		15. SECURITY CLASS *(of this report)* UNCLASSIFIED 15a. DECLASSIFICATION DOWNGRADING SCHEDULE

16. DISTRIBUTION STATEMENT *(of this Report)*

Approved for public release; distribution unlimited.

17. DISTRIBUTION STATEMENT *(of the abstract entered in Block 20, if different from Report)*

18. SUPPLEMENTARY NOTES

This work sponsored by the Defense Nuclear Agency under RDT&E RMSS Code B310080464 P99QAXDB00157 H2590D.

19. KEY WORDS *(Continue on reverse side if necessary and identify by block number)*

EMP
Ivy Mike
Lightning
Nuclear Explosions
Radiation
Source Region EMP

20. ABSTRACT *(Continue on reverse side if necessary and identify by block number)*

Analytic solutions and numerical results are obtained for three models for quasi-static source region EMP from a nuclear surface burst, representing electron-dominated air conductivity, ion-dominated air conductivity, and an intermediate situation with electron-dominated conductivity at short ranges and ion-dominated conductivity at long ranges. Comparisons are made with the results of previous approximate analyses and with the gross features of lightning strokes which were observed in the 1- to 10-ms time frame on the Mike shot.

DD FORM 1 JAN 73 1473 EDITION OF 1 NOV 65 IS OBSOLETE

UNCLASSIFIED

SECURITY CLASSIFICATION OF THIS PAGE *(When Data Entered)*

20. ABSTRACT (Continued)

Uncertainties in air chemistry and ionization rate parameters give rise to roughly ± 50 percent uncertainties in electric field strength and roughly factor-of-three uncertainties in the applicable time frame for each of the above-mentioned models. Within these uncertainties, the EMP predictions appear to be consistent with the gross features of the observed lightning.

SUMMARY

Analytic solutions and numerical results are obtained for three models for quasi-static source region EMP from a nuclear surface burst, representing electron-dominated air conductivity, ion-dominated air conductivity, and an intermediate situation with electron-dominated conductivity at short ranges and ion-dominated conductivity at long ranges. Comparisons are made with the results of previous approximate analyses and with the gross features of lightning strokes which were observed in the 1- to 10-ms time frame on the Mike shot. Uncertainties in air chemistry and ionization rate parameters give rise to roughly ±50 percent uncertainties in electric field strength and roughly factor-of-three uncertainties in the applicable time frame for each of the above-mentioned models. Within these uncertainties, the EMP predictions appear to be consistent with the gross features of the observed lightning.

PREFACE

It is a pleasure to acknowledge the substantial contributions made to this work by Drs. Carl Greifinger, Phyllis Greifinger, and William Karzas.

TABLE OF CONTENTS

LIST OF ILLUSTRATIONS

LIST OF ILLUSTRATIONS (CONTINUED)

I. INTRODUCTION

This report has two objectives. The first is to present some new analytic solutions for source region EMP from a surface nuclear burst over a perfect ground in the quasi-static time regime, the late-time period during which time derivatives in Maxwell's equations can be neglected. The second objective is to compare the existing theory of source region EMP, as embodied in these analytic solutions, with the gross features of lightning strokes observed on the Mike shot (Ref. 1).

Quasi-static source region EMP has been investigated previously by Longmire (Ref. 2), Hill (Ref. 3) and Wyatt (Ref. 4), all of whom noted that the radial component of the electric field would be smaller than the polar component, and therefore assumed that it could be neglected in the calculations. In the present work no such approximation is made. The electrostatic potential is expanded in spherical harmonics (Legendre polynominals) to obtain a set of ordinary differential equations for the radial functions appearing in the expansion. Simple air conductivity models are introduced for the early-time regime when the conductivity is dominated by electrons (Model 1), the late-time regime when ions dominate (Model 2), and for the intermediate time regime when electrons dominate the conductivity close to the burst but ions dominate farther away (Model 3). Using these simple models, analytic solutions are obtained for the required radial functions. The results are then evaluated numerically using a programmable calculator.

From the present work it is found that neglect of the radial component of the electric field is not justified when electrons contribute significantly to the air conductivity. In addition, it is found (from Model 2) that even in the special

case where ions dominate the air conductivity, the previous approximate solutions obtained by the above-referenced authors are only qualitatively correct. The results from Model 1 and Model 3 provide new insight into the electromagnetic field structure when electron conductivity cannot be neglected.

Concerning the application to nuclear lightning, it has previously been asserted (Refs. 5–8) that the gross characteristics of lightning observed on the Mike shot are clearly inconsistent with the existing theory of source region EMP. This assertion has been based on the assumptions that (1) the lightning requires fields greater than 100 kV/m, whereas the EMP theory predicts fields of the order of ~10–50 kV/m, and that (2) the observed curvature of the lightning strokes cannot be explained unless ionic air conductivity dominates over electronic conductivity to a degree significantly greater than the existing EMP theory would allow. Based on these assumptions, it has been concluded by others that the observed lightning provides evidence for an anomalously rapid electron attachment mechanism, which lowers electron conductivity and leads to higher EMP field strengths.

In the present report it is shown that these assumptions do not appear to be well founded, for a number of reasons. First, it is pointed out that existing data do not confirm the hypothesized 100-kV/m criterion for lightning stroke initiation, even under nonnuclear conditions, and that the presence of ionized, conducting air may also facilitate leader development in the EMP source region. Furthermore, it is found that the observed lightning stroke curvature cannot be shown to be inconsistent with the existing EMP theory because of (1) the hitherto unrecognized dominance of the polar component of the electric field even earlier than the onset of ion conductivity dominance, (2) the continual decline in the importance of electron conductivity during the period of

lightning stroke evolution, and (3) the uncertainties in the present theory regarding the relative contributions of electrons and ions to the source region air conductivity at late times. Thus, it is concluded that the gross features of the observed lightning may very well be consistent with the existing theory of source region EMP. Although the possibility of some anomalous electron attachment mechanism cannot be ruled out, the present comparison of theory and observation does not find evidence in support of its existence.

II. THE MODELS

For times later than about 10 μs after a low-altitude nuclear burst, the rate of change of the Compton current becomes so low that it is commonly assumed (Refs. 2-5) that the electromagnetic fields attain a quasi-static equilibrium in which all time derivatives in Maxwell's equations can be neglected and time treated as a parameter rather than an independent variable. Then, since

$$\vec{\nabla} \times \vec{E} = -\dot{\vec{B}} \simeq 0 ,$$

the electric field is derivable from a potential

$$\vec{E} = -\vec{\nabla}\Phi .$$

And since

$$\vec{\nabla}\cdot(\sigma\vec{E} + \vec{J}_c) = -\dot{\rho} \simeq 0$$

(where σ is the air conductivity, $\vec{J}_c$ the Compton current density and ρ the charge density), the potential is determined by the equation

$$\vec{\nabla}\cdot(\sigma\vec{\nabla}\Phi) = \vec{\nabla}\cdot\vec{J}_c \qquad (1)$$

subject to the boundary conditions that $\vec{E}$ be finite at the origin and zero at infinity and (for a perfectly conducting earth) that the tangential component of $\vec{E}$ vanish at the surface of the earth.

In the present work we will assume (Ref. 5) that the Compton current from a nuclear surface burst may be approximately represented as

$$\vec{J}_c = \hat{r} J_o e^{-r/\lambda}/r^2 \tag{2}$$

where $\hat{r}$ is a unit vector in the radial direction, r is the distance from the origin and λ an effective γ-ray mean free path. Monte Carlo studies (Refs. 9,10) indicate that the theta component of $\vec{J}_c$ will generally be substantially less than the radial component, except at $r \lesssim \lambda$.

The air conductivity σ will involve contributions from both electrons and ions. In a quasi-steady-state situation the electron contribution will be of the form (Refs. 5,11)

$$\sigma_e = e\mu_e S/\alpha \tag{3}$$

where e is the electronic charge, μ_e the electron mobility, S the local ionization rate and α the electron attachment rate. The quasi-steady-state form for ionic conductivity will be (Ref. 5)

$$\sigma_I = 2e\mu_I (S/k)^{1/2} \tag{4}$$

where μ_I is the average ion mobility and k the ion-ion recombination rate constant. The spatial variation of $\sigma = \sigma_e + \sigma_I$ will thus be determined by the spatial variation of the ionization rate, which we will assume (Ref. 5) to be of the form

$$S = S_o e^{-r/\lambda}/r^2 \quad . \tag{5}$$

In addition, the electron mobility and attachment rate will vary weakly with the local value of the electric field strength (Ref. 11). However, we will assume that this variation can be neglected in solving Eq. (1), provided only that the values of μ_e and α used in the final analysis are consistent with the calculated average local electric-field strength in the region considered. This is reasonable since the ratio μ_e/α, in Eq. (3) is nearly independent of electric-field in most situations of interest.

Equations (3-5) imply a rather complex dependence of the total conductivity on range, with $\sigma_e \sim e^{-r/\lambda}/r^2$ dominating at short ranges (high dose rate) and $\sigma_I \sim e^{-r/2\lambda}/r$ dominating at larger ranges (low dose rate). However, at sufficiently early times and/or for larger yield explosions, the source strength (S_o) will be large enough that the domination of σ_e over σ_I will continue out to ranges of many gamma mean free paths. In order to investigate the close-in source region EMP fields under these conditions we will adopt a model in which σ_I is ignored altogether.

$$\text{Model 1 (M1):} \quad \sigma(r) = \sigma_o \, e^{-r/\lambda}/r^2 \, , \tag{6}$$

and σ_o will scale in proportion to the source strength S_o [defined by Eq. (5)].

Similarly, at sufficiently late times and/or for lower yield explosions, the source strength will be so low that σ_I will dominate over σ_e everywhere except within a few hundred meters of the detonation point. For this situation we will adopt a model in which σ_e is ignored altogether.

$$\text{Model 2 (M2):} \quad \sigma(r) = \sigma_o \, e^{-r/2\lambda}/r\lambda \, , \tag{7}$$

and σ_o will scale as the square root of S_o.

Finally, for the intermediate situation where σ_e dominates out to $r \simeq 1$ km or so, with σ_I dominating at the larger ranges, we note that since λ is typically about 300 m, $\sigma(r)$ varies approximately as $1/r^2$ at the shorter ranges ($r \lesssim 1$ km) and approximately as $e^{-r/2\lambda}$ at the longer ranges ($r \gtrsim 1500$ m). For this situation we adopt a simplified conductivity model which exhibits this dominant behavior:

$$\text{Model 3 (M3):} \quad \sigma(r) = \sigma_o e^{-r/2\lambda}/r^2. \tag{8}$$

Here the value of σ_o must be obtained by a fit to the estimated true form of $\sigma(r) = \sigma_e(r)+\sigma_I(r)$. Such a fit is shown in Figure 1 for the case of a 10-MT surface burst at $t \simeq 1$ ms. The parameters used in constructing these curves will be discussed later.

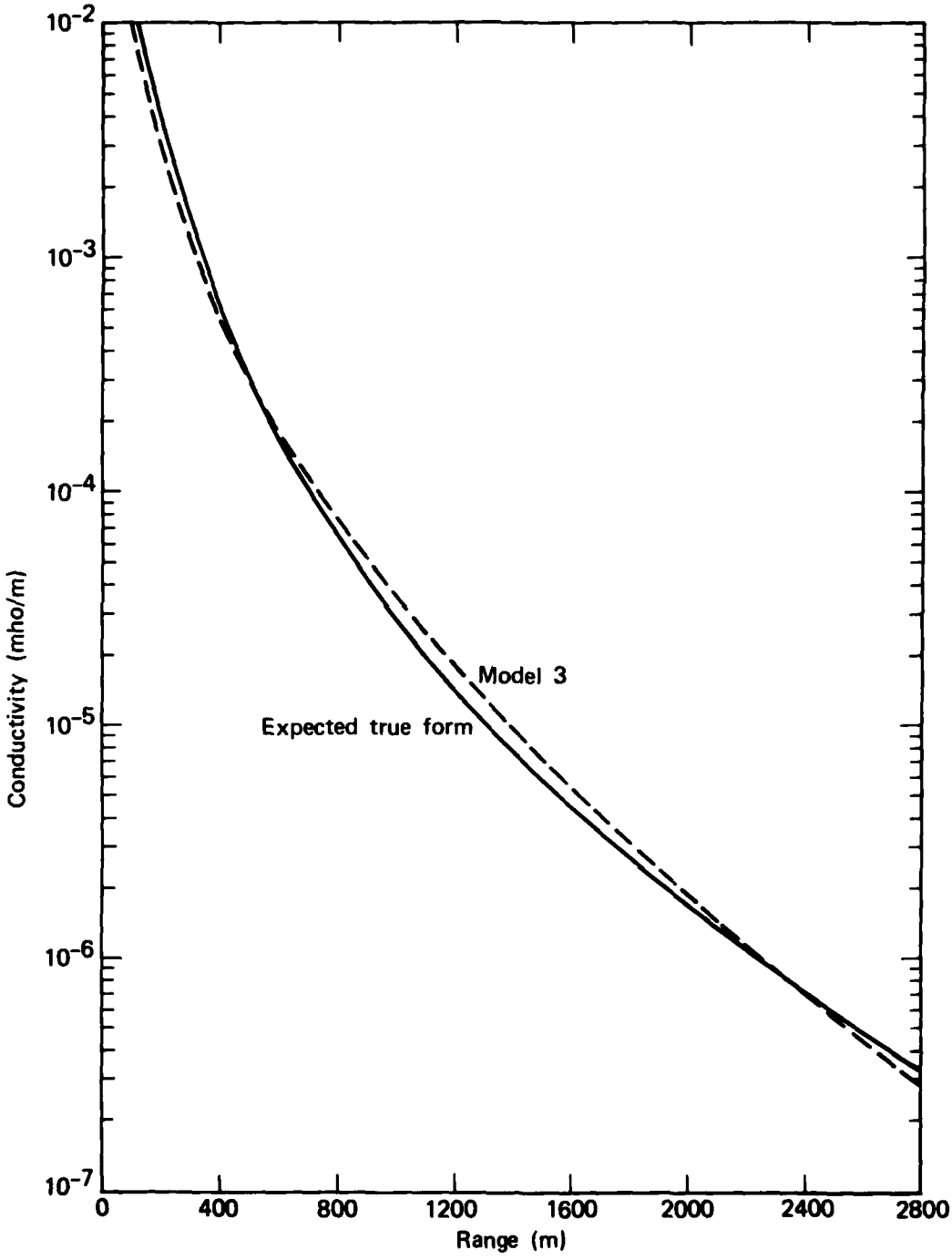

Figure 1. Comparison of Model 3 to expected conductivity for 10-MT burst at $t \simeq 1$ ms.

III. THE SOLUTIONS

Equation (1) can be rewritten in spherical coordinates as (we ignore a $\delta(r)$ on the right-hand side which does not effect the solution for $r \neq 0$)

$$\frac{1}{r^2}\frac{\partial}{\partial r}\left(r^2\sigma(r)\ \frac{\partial}{\partial r}\ \Phi(r,\theta)\right) + \frac{\sigma(r)}{r^2\ \sin\ \theta}\frac{\partial}{\partial\theta}\left(\sin\ \theta\ \frac{\partial}{\partial\theta}\ \Phi(r,\theta)\right) =$$

$$-\frac{1}{\lambda}\left(\hat{r}\cdot\vec{J}(r)\right). \tag{9}$$

The angle θ is measured from the vertical, so that $\theta = 0$ directly above the burst and $\theta = \pi/2$ at the surface of the earth. For $0 \leq \theta < \pi/2$ the θ-independent right-hand side of Eq. (9) may be written as (Ref. 12)

$$-\frac{1}{\lambda}\left(\hat{r}\cdot\vec{J}(r)\right) = -\frac{1}{\lambda}\left(\hat{r}\cdot\vec{J}(r)\right)\sum_{i=0}^{\infty} A_{2i+1}\ P_{2i+1}(\cos\ \theta)$$

where the $P_{2i+1}(\mu)$ are Legendre polynomials and ($\ell \equiv 2i+1$)

$$A_\ell = \left(\frac{1}{2}\right)^{(\ell-1)/2}\left(\frac{(2\ell+1)\,(\ell-2)!!}{2\left(\frac{\ell+1}{2}\right)!}\right) \tag{10}$$

If we also represent $\Phi(r,\theta)$ as

$$\Phi(r,\theta) = \sum_{i=0}^{\infty}\phi_{2i+1}(r)\ P_{2i+1}\ (\cos\ \theta) \tag{11}$$

Then the boundary condition on E_r at $\theta = 90°$ is met automatically and

$$\frac{d^2}{dr^2}\,\phi_\ell(r) + \frac{2}{r}\,\frac{d}{dr}\,\phi_\ell(r) + \frac{1}{\sigma(r)}\left(\frac{d\sigma(r)}{dr}\right)\frac{d\phi_\ell(r)}{dr}$$

$$- \frac{\ell(\ell+1)}{r^2}\,\phi_\ell(r) = -\frac{A_\ell}{\lambda}\,\frac{\hat{r}\cdot\vec{J}(r)}{\sigma(r)}\,. \qquad (12)$$

From the defining Eqs. (2,6,7,8) we may then introduce

$$\frac{1}{\sigma(r)}\,\frac{d}{dr}\,\sigma(r) = \begin{cases} -\left(\frac{1}{\lambda} + \frac{2}{r}\right) & \text{(M1)} \quad (13a) \\ -\left(\frac{1}{2\lambda} + \frac{1}{r}\right) & \text{(M2)} \quad (13b) \\ -\left(\frac{1}{2\lambda} + \frac{2}{r}\right) & \text{(M3)} \quad (13c) \end{cases}$$

and

$$\hat{r}\cdot\vec{J}(r)/\sigma(r) = \begin{cases} (J_o/\sigma_o) & \text{(M1)} \quad (14a) \\ (J_o/\sigma_o)\,\frac{\lambda}{r}\,e^{-r/2\lambda} & \text{(M2)} \quad (14b) \\ (J_o/\sigma_o)\,e^{-r/2\lambda} & \text{(M3)} \quad (14c) \end{cases}$$

into (12) to obtain the appropriate radial equation for each model.

For Model 1 the homogeneous equation corresponding to Eq. (12) has two independent solutions (Ref. 13) of the form

$$\phi_{\ell 1}(r) = \sqrt{r/2\lambda}\, e^{r/2\lambda}\, I_{\ell+1/2}(r/2\lambda) \tag{15a}$$

$$\phi_{\ell 2}(r) = \sqrt{r/2\lambda}\, e^{r/2\lambda}\, K_{\ell+1/2}(r/2\lambda) \tag{15b}$$

where $I_{\ell+1/2}(x)$ and $K_{\ell+1/2}(x)$ are modified spherical Bessel functions. The solution to Eq. (12) is then given by

$$\phi_{\ell}(r) = 4\lambda A_{\ell}(J_o/\sigma_o)\sqrt{r/2\lambda}\, e^{r/2\lambda}\left[I_{\ell+1/2}(r/2\lambda)\int_{r/2\lambda}^{\infty} dy\, K_{\ell+1/2}(y)\sqrt{y}\, e^{-y}\right.$$
$$\left. + K_{\ell+1/2}(r/2\lambda)\int_{0}^{r/2\lambda} dy\, I_{\ell+1/2}(y)\sqrt{y}\, e^{-y}\right] . \tag{16}$$

It can be shown from Eq. (16) that $\phi_{\ell}(r)$ behaves like r^2 [or $r^2 \ell n(r)$ for $\ell = 1$] as $r \to 0$ and like r as $r \to \infty$. Note that this result (and the basic model as well) is somewhat unphysical in that the electric field is nonzero at $r \to \infty$. This is at least partially a result of the unphysical assumption that $\sigma_I << \sigma_e$ (so that $\hat{r}\cdot\vec{J}/\sigma$ = a constant) even as $r \to \infty$. However, we will only apply Model 1 at short ranges from the burst, where $\sigma_e >> \sigma_I$.

For Model 2, the homogeneous variant of Eq. (12) has two independent solutions of the form (Ref. 14)

$$\phi_{\ell 1}(r) = r^p\, M(p, 2p+1, r/2\lambda) \tag{17a}$$

$$\phi_{\ell 2}(r) = r^p\, U(p, 2p+1, r/2\lambda) \tag{17b}$$

where $p = \sqrt{\ell(\ell+1)}$ and $M(p,2p+1,r/2\lambda)$ and $U(p,2p+1,r/2\lambda)$ are confluent hypergeometric functions. The solution to Eq. (12) may then be written as [$\Gamma(p)$ is the gamma function]

$$\phi_\ell(r) = \lambda A_\ell \left(\frac{J_o}{\sigma_o}\right) \frac{\Gamma(p)}{p\Gamma(2p)} \, (r/2\lambda)^p$$

$$\times \left[M(p,2p+1,r/2\lambda) \int_{r/2\lambda}^{\infty} dy \; U(p,2p+1,y) y^p e^{-2y} \right.$$

$$\left. + \, U(p,2p+1,r/2\lambda) \int_0^{r/2\lambda} dy \; M(p,2p+1,y) y^p e^{-2y} \right] . \qquad (18)$$

From Eq. (18) it can be shown that $\phi_\ell(r)$ behaves like r as $r \to 0$ and like a constant as $r \to \infty$. In this case the electric field vanishes at $r = \infty$.

Finally, for Model 3, the homogeneous equation corresponding to Eq. (12) has independent solutions (Ref. 13)

$$\phi_{\ell 1}(r) = \sqrt{r/4\lambda} \, e^{r/4\lambda} I_{\ell+1/2}(r/4\lambda) \qquad (19a)$$

$$\phi_{\ell 2}(r) = \sqrt{r/4\lambda} \, e^{r/4\lambda} K_{\ell+1/2}(r/4\lambda) \qquad (19b)$$

The solution to Eq. (12) is then given by

$$\phi_\ell(r) = 16A_\ell\lambda\left(\frac{J_o}{\sigma_o}\right)\sqrt{r/4\lambda}\; e^{r/4\lambda}$$

$$\times\left[I_{\ell+1/2}(r/4\lambda)\int_{r/4\lambda}^{\infty} dy\; K_{\ell+1/2}(y)\sqrt{y}\; e^{-3y}\right.$$

$$\left. + K_{\ell+1/2}(r/4\lambda)\int_{0}^{r/4\lambda} dy\; I_{\ell+1/2}(y)\sqrt{y}\; e^{-3y}\right] . \qquad (20)$$

In this case $\phi_\ell(r)$ behaves like r^2 (or r^2 ℓn r) as $r \to 0$ and like a constant as $r \to \infty$, thus the electric field vanishes at $r \to \infty$.

The Eqs. (10,11,16,18,20) provide a set of exact closed-form solutions for each of our three models. The electric fields can then be obtained from the equations

$$E_\theta = \frac{\sin\theta}{r}\sum_{i=0}^{\infty}\phi_{2i+1}(r)\left(\frac{d}{d(\cos\theta)}P_{2i+1}(\cos\theta)\right) \qquad (21)$$

$$E_r = -\sum_{i=0}^{\infty}\left(\frac{d}{dr}\phi_{2i+1}(r)\right)P_{2i+1}(\cos\theta) . \qquad (22)$$

In Eq. (22) we must have expressions for $d\phi_\ell(r)/dr$ for each model ($\ell \equiv 2i+1$). These can be found easily by differentiating Eqs. (16, 18, 20) and using recursion relations (Refs. 13, 14) for the derivatives of the special functions.

IV. PHYSICAL RESULTS

In order to generate specific results for the electric fields predicted by each model, we must choose numerical values for the parameters λ, J_o and σ_o. The value of σ_o will, of course, be different for each of the three models.

Here we will take $\lambda = 320$ m for the effective gamma dose attenuation length. For the Compton current, a review of the Monte Carlo calculations by Sargis et al. (Ref. 9) indicates that at $t \sim 1$ ms and $500 \text{ m} \lesssim r \lesssim 2900$ m

$$\hat{r}\cdot\vec{J}_c(A/m^2) \simeq -5.6 \times 10^{-24} \, S(\text{ion-pairs}/m^3/s)$$

where S is the local ionization rate. On the other hand, the Monte Carlo calculations by the Mathematical Applications Group, Inc. (MAGI) (Ref. 10) are more consistent with a proportionality

$$\hat{r}\cdot\vec{J}_c(A/m^2) \simeq -1.2 \times 10^{-23} \, S(\text{ion-pairs}/m^3/s).$$

For the present, we will use an intermediate value, choosing

$$\hat{r}\cdot\vec{J}_c(A/m^2) = -8.2 \times 10^{-24} \, S(\text{ion-pairs}/m^3/s). \qquad (23)$$

And the uncertainty associated with this value is evidently at least ± 40 percent.

In the electron conductivity [see Eq. (3)] we will use (Ref. 11)

$$\alpha = 1.5 \times 10^8 \ s^{-1}$$

$$\mu_e = 0.25 \ m^2/V\text{-}s \ .$$

These values are appropriate for electric field strengths of a few tens of kilovolts per meter (kV/m) and air with ∿2 percent moisture content. They are each thought to be uncertain by ±30 to 40 percent. From Eq. (3) we then obtain (the electric field dependence of the ratio μ_e/α is not important in slightly moist air)

$$\sigma_e(\text{mho/m}) = 2.7 \times 10^{-2\delta}\ S(\text{ion-pairs/m}^3/\text{s}). \qquad (24)$$

Using these numerical values in Model 1 (electron-dominated conductivity) we obtain

$$\text{M1:}\quad J_o/\sigma_o = -30\ \text{kV/m}$$

a value which must be regarded as uncertain by at least ±50 percent. With this value of J_o/σ_o and λ = 320 m, the calculated electric fields for Model 1 are shown in Figure 2. The radial field E_r is calculated at $\theta = 0°$ and the polar field E_θ $\theta = 90°$ (at the ground), since they are each expected to have their largest values at these angles.

In the ionic conductivity [see Eq. (4)] we will use the values (Refs. 5,15)

$$k = 2 \times 10^{-12}\ \text{m}^3/\text{s}$$

$$\mu_I = 2.6 \times 10^{-4}\ \text{m}^2/\text{V-s}$$

and we roughly estimate the uncertainties of these values to be about ±30 percent (for μ_I) to ±50 percent (for k). From Eq. (4) we have

$$\sigma_I(\text{mho/m}) = 5.9 \times 10^{-17}\ S(\text{ion-pairs/m}^3/\text{s})^{1/2}\ . \qquad (25)$$

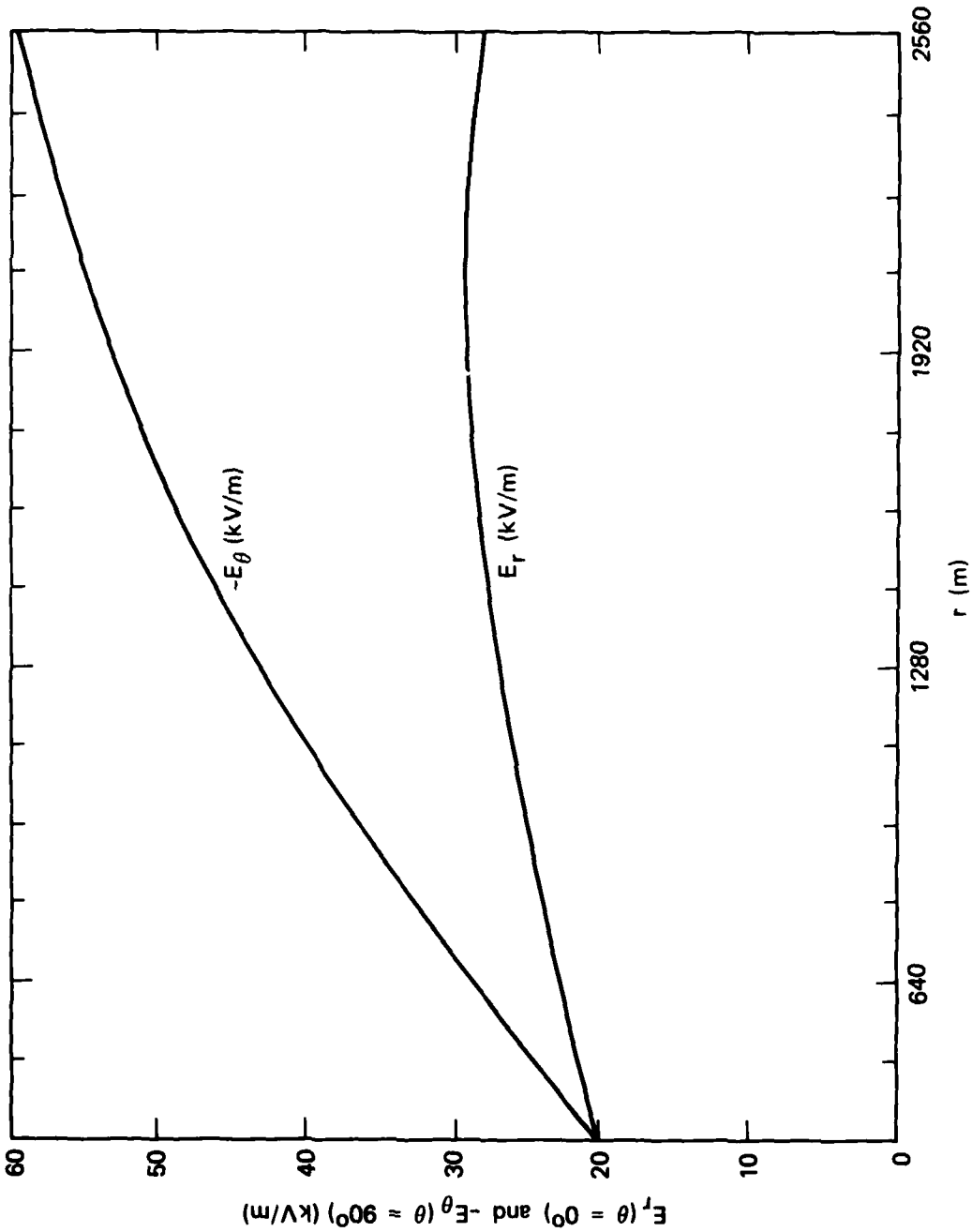

Figure 2. Numerical results from Model 1 for $E_r(\theta = 0^o)$ and $-E_\theta(\theta = 90^o)$ (assumes λ = 320 m, $-J_o/\sigma_o \approx$ 30 kV/m).

For Model 2 (ion-dominated conductivity) the ratio (J_o/σ_o) will be proportional to $S_o^{1/2}$, which is essentially the square root of the source strength [see Eq. (5)]. From a review of the Monte Carlo results (Refs. 9,10) we find a value of S_o at $t \sim 30$ ms for a 10-MT burst, assuming 2×10^{26} source neutrons per MT (Refs. 16, 17), of S_0 (30 ms) $\simeq 7.2 \times 10^{28}$ ion-pairs/m/s. For this particular case we then obtain a value of J_0/σ_0 for Model 3 (again with at least $\pm$50 percent uncertainty)

$$\text{M2:} \quad (J_o/\sigma_o) = -116 \text{ kV/m}.$$

The electric fields E_r ($\theta = 0°$) and E_θ($\theta = 90°$) calculated from Model 2 with this value of J_o/σ_o and $\lambda = 320$ m are shown in Figure 3. For other burst yields and/or times after detonation, the appropriate value of S_o will be different and the fields will scale as $S_o^{1/2}$.

It is also important to compare the calculated values of $\sigma_e(r)$ and $\sigma_I(r)$ at some fairly close-in range, say r = 500 m, for this choice of S_o. We find σ_e (500 m) $\simeq \sigma_I$(500 m) $\simeq 1.5 \times 10^{-5}$ mho/m. Clearly, Model 2 would be of questionable validity for much higher values of S_o. Note, however, that for substantially lower yields Model 2 would become applicable at much earlier times, perhaps as early as ~30 μs for a 20-KT burst (however, the displacement current will also start to become important for such low yields and early times). The presence of a highly conducting expanding fireball would also detract from the applicability of the model for very large yields. For a 10-MT burst at $t \sim 30$ ms, the fireball will have reached about 500 m.

As for the limits of applicability of Model 1 we may note from the Monte Carlo work (Refs. 9,10) that the source strength at t ~ 30 μs for a 10-MT burst would be about

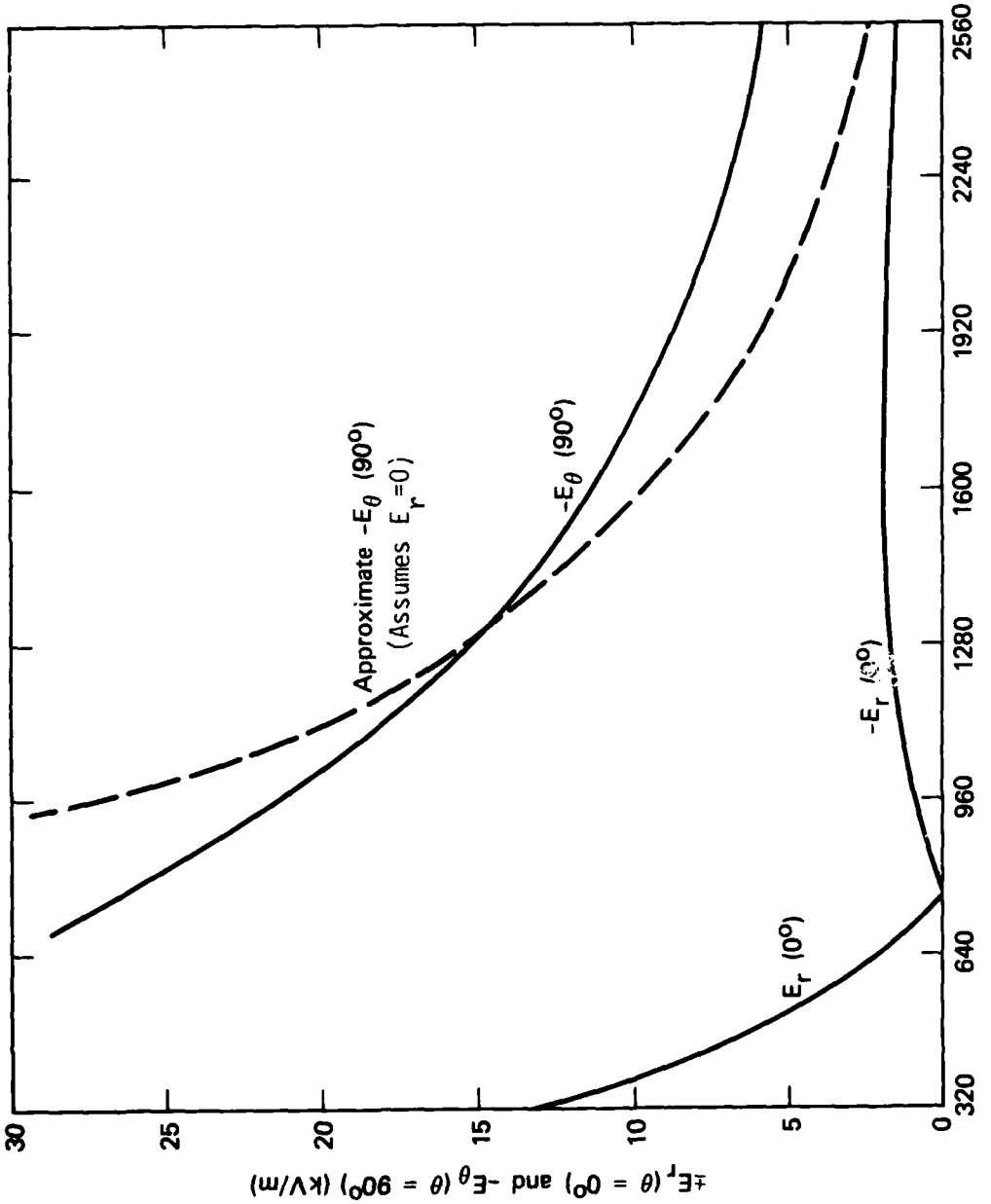

Figure 3. Numerical results from Model 2 for $\pm E_r(0^o)$ and $-E_\theta(90^o)$ (assumes λ = 320 m, $-J_o/\sigma_o$ = 116 kV/m).

2.5×10^{31} ion-pairs/m/s. For this value of S_o the electronic and ionic contributions become comparable at r = 1700 m. Thus, even for a 10-MT burst, Model 1 must have a fairly limited range of applicability (i.e., $t \lesssim 30$ μs, $r \lesssim 1500$ m). For lower yields (lower S_o) the requirement that σ_e dominate over σ_I will be even more restrictive.

Model 3 is intended to at least partially bridge the gap between Models 1 and 2. As shown in Figure 1, this model provides a good fit to the total conductivity from a 10-MT burst at $t \sim 1$ ms. The source strength used in Figure 1 was $S_o = 1.1 \times 10^{30}$ ion-pairs/m/s. At this source strength the electron and ion conductivities become comparable at about 1 km. Fitting the model form of the conductivity to the expected true form gave

$$\text{M3:} \quad J_o/\sigma_o = -63 \text{ kV/m} .$$

The electric fields E_r (0°) and E_θ (90°) calculated from Model 3 with this value of J_o/σ_o are displayed in Figure 4.

In order to examine the limits of validity of Model 3, we have shown in Figure 5 a fit of the model form of the conductivity to the expected true form for $S_o = 1.6 \times 10^{30}$ ion/pairs/m/s and for $S_o = 3.6 \times 10^{29}$ ion-pairs/m/s, appropriate for a 10-MT burst at $t \sim 300$ μs and $t \sim 3$ ms, respectively. It may be seen that the model still provides a fair fit, differing from the desired form by less than 50 percent over a range of five orders of magnitude in conductivity. Thus, for a 10-MT burst, we might expect the electric fields to exhibit a qualitative similarity to those shown in Figure 5 for the interval $300 \text{ μs} \lesssim t \lesssim 3$ ms. Also, since the value of σ_o used for these fits decreases by about a factor of 3.3 from $t \simeq 300$ μs to $t \simeq 3$ ms, while S_o (and J_o) decreases by a factor of 4.4, the EMP fields (proportional to J_o/σ_o) are changing very slowly in magnitude.

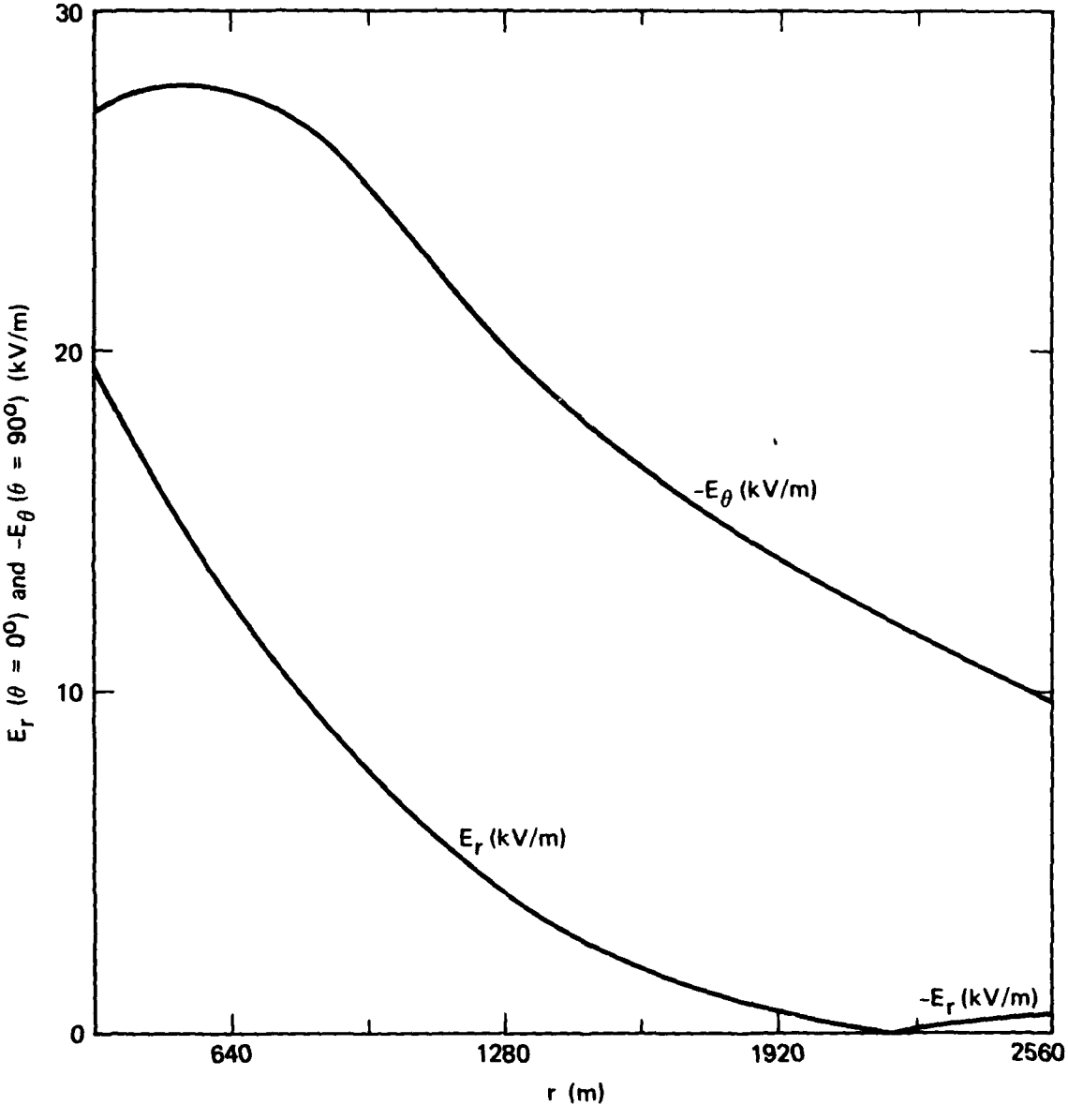

Figure 4. Results from Model 3 for E_r and $-E_\theta$ (assumes λ = 320 m, $-J_o/\sigma_o$ = 63 kV/m).

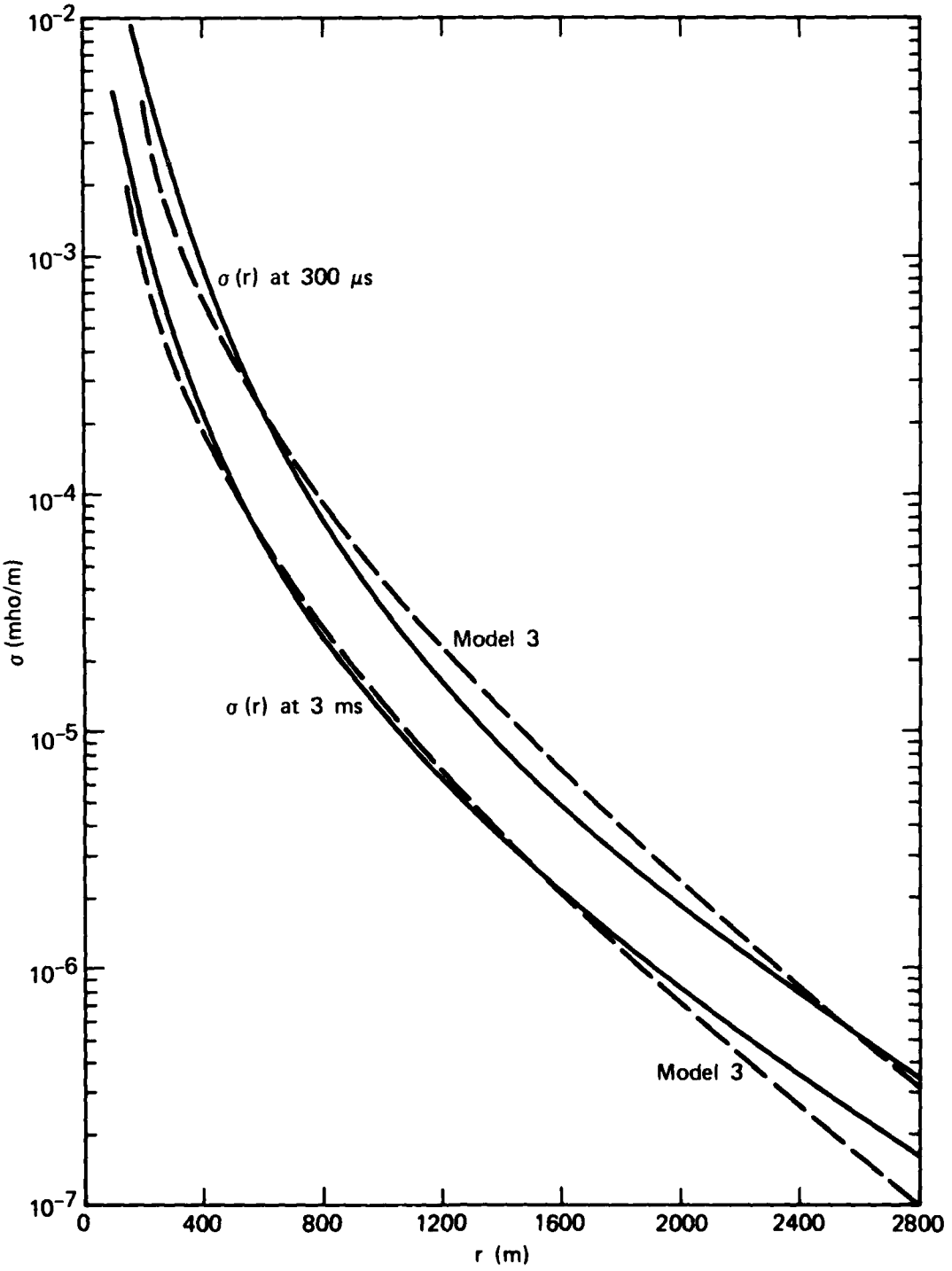

Figure 5. Comparison of Model 3 to expected true form for a 10-MT burst at t ~ 300 μs and at t ~ 3 ms.

Finally, we must address the limits of applicability of the quasi-static hypothesis, upon which all of the present calculations have been based. There are two conditions. The displacement current must be much less than the conduction current; e.g., $\sigma/\varepsilon >> t^{-1}$. Also, the electric field must be derivable from a scalar potential. The first condition is more easily met for large yields at short ranges and late times. It becomes marginal for a 10-MT burst at $t \lesssim 3$ μs and $r \gtrsim 3$ km. For a 20-KT burst, the condition becomes marginal at $t \lesssim 30$ μs and $r \gtrsim 2$ km. The second condition can be shown to reduce to a requirement that $\sigma << t/\mu_o \lambda^2$, where μ_o is the permeability of free space. This condition is more easily met for lower yields at later times and larger ranges. For a 10-MT burst it becomes marginal at $t \lesssim 100$ μs and $r \lesssim 1$ km. For a 20-KT burst it becomes marginal at $t \lesssim 100$ μs and $r \lesssim 500$ m. It may be seen that this last condition, combined with the requirement that $\sigma_e >> \sigma_I$, appears to place a very severe restriction on the applicability of M1.

V. COMPARISON WITH OTHER WORK

Longmire (Ref. 2) was apparently the first to address the problem of quasi-static source region EMP. He developed an approximate solution to Model 2 by noting that E_r should be very small, also changing sign at $r \simeq 2\lambda$. On this basis, an explicit expression was obtained for the azimuthal magnetic field at $\theta = 90°$.

$$B_\phi = r\left(\hat{r}\cdot\vec{J}_c(\vec{r})\right) \quad .$$

In analogous developments, Hill (Ref. 3) and later Wyatt (Ref. 4) also gave approximate expressions for the polar electric field. Wyatt's result, including a polar component of J_c, is

$$E_\theta = -\frac{1}{\sigma}\left[J_{c\theta} - \frac{r}{\lambda}\tan(\theta/2)J_{cr}\right].$$

This approximation is also plotted in Figure 3 as the dashed line. It may be seen that the approximate result is fairly reasonable, particularly in those regions where E_r and dE_r/dr are smallest.

Hill applied this result to estimate E_θ for a 10-MT burst, at $t \simeq 3$ ns, but assumed a substantially lower dose rate than would be indicated by the Monte Carlo work (e.g., Hill uses $S_o \simeq 2.4 \times 10^{28}$ ion-pairs/m/s, compared to $S_o \simeq 3.6 \times 10^{29}$ ion-pairs/m/s from the Monte Carlo work.) Because of this assumed dose rate, the ion conductivity was dominant in Hill's problem, as required for Model 2 to apply.

In Wyatt's application of the approximate solution to Model 2, a source strength of $S_o = 7.2 \times 10^{29}$ ion-pairs/m/s was assumed for a 10-MT burst at t ~ 10 ms. This dose rate is about 3 to 4 times larger than would be indicated by the Monte Carlo work. At this dose rate Model 3, with both ionic and electronic contributions to the air conductivity, should have been used rather than the approximate solution to Model 2. Also, it appears that Wyatt miscalculated the ionic conductivity by a factor of 2, apparently not including the contributions of both positive and negative ions, and used an anomalously large ion-ion recombination rate for clustered ions.

VI. APPLICATION TO NUCLEAR LIGHTNING

This work was motivated primarily by the recent interest (Refs. 3-8) in lightning strokes triggered by nuclear explosions (Ref. 1). On the Mike shot, a 10-MT surface burst, five lightning strokes were observed at ranges from 900 m to 1380 m from ground zero. The lightning strokes began near the ground, apparently at $t \lesssim 1$ ms, and travelled upward following roughly concentric paths about the burst point throughout the time frame of 1 ms $\lesssim t \lesssim$ 10 ms. It is thought that they may have been initiated at the tips of communications antennas or other structures at varying distances from ground zero. A detailed drawing (Ref. 1) showing the progression of the brightest stroke (at r = 900 m) is given in Figure 6. In every case, the cloud level was low enough that the strokes could not be observed at elevations higher than 30° to 45° above the horizontal, as viewed from the burst point. Also, a photograph taken at 36 ms indicates (Ref. 1) that only one of the strokes actually reached cloud level.

From a study of several examples of triggered ground-to-cloud lightning under nonnuclear conditions, Pierce (Ref. 18) proposed an empirical rule that $E_o h$ = (ambient field) x (structure height) $\gtrsim$ 1 MV. Such a scaling of field strength vs structure height does not seem implausible, since the potential drop within a few structure radii of the tip is also of the order of $E_o h$, and this potential drop should be important in initiating any discharge. Pierce's rule, with an assumed structure height (h) of $\simeq$10 m, led Uman et al. (Ref. 1) to suggest that a 100-kV/m EMP field would be needed to explain

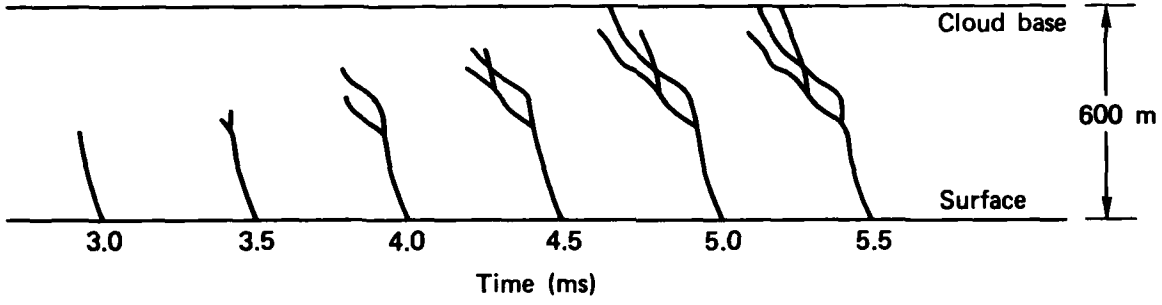

Figure 6. The vertical development of the lightning discharge. Drawing made by tracing prints of six frames of a high-speed movie of the detonation. (Ref. 1)

the Mike lightning (assuming that the radiation-induced ionization is unimportant). However, Pierce's data set did not include any relevant examples of triggered lightning with $h \lesssim 100$ m. (One example at $h = 70$ m apparently had no real data on E_o. Two other examples of lightning strikes to in-flight aircraft having dimensions of 5 to 36 m gave $E_o h \simeq 36$-75 kV, a factor of 13 to 28 lower than the proposed 1-MV criterion!) The remaining examples generally appear to conform to Pierce's suggested rule, but show a scatter of about a factor of 3 in $E_o h$, while E_o ranges only from 3 kV/m to 20 kV/m and h varies only from 100 m to 400 m.

Overall, it cannot be said that the data demonstrate the validity of a scaling law of the form $E_o h \simeq$ constant for triggered lightning, or that they can be extrapolated with better than order-of-magnitude accuracy to estimate the value of E_o needed to trigger lightning from a structure with $h \simeq 10$ m. Furthermore, after having examined a variety of empirical schemes for plotting and extrapolating the data cited by Pierce, this author holds the view that they are not inconsistent with a required field strength anywhere in the general range $15 \text{ kV/m} \lesssim E_o \lesssim 150 \text{ kV/m}$ for triggered lightning from a structure with $h \simeq 10$ m. The EMP fields which we have just calculated are certainly within this range, particularly when we recall that the values of J_o/σ_o employed are probably uncertain by at least ± 50 percent.

It clearly would be very useful to have data on the presence or absence of upward propagating strokes from structures with $h \lesssim 10$ m in ambient fields of the order of 20 kV/m to 100 kV/m. However, field strengths at the earth's surface beneath storm clouds do not frequently exceed 20 kV/m (Ref. 19), and triggered ground-to-cloud strokes from structures with

$h \lesssim 10$ m are apparently also very uncommon. Thus, it may be difficult to find data in the regime of interest from observations of naturally occurring ground-to-cloud lightning (the absence of massive nuclear radiation would also be a concern).

Stronger surface fields do arise when a cloud-to-ground stroke approaches the earth, and such fields very commonly trigger upward-propagating *connecting leaders* from short ($h \lesssim 10$ m) grounded conductors. This is, in fact, the protective mechanism of the lightning rod. It is generally believed (Refs. 19,20) that such upward strokes will begin when the enhanced field at the conductor tip reaches about 3 MV/m. In an ambient field of 30 kV/m, this would require a prolate spheroidal structure (Ref. 21) with an aspect ratio of $h/r \simeq 20$.

Although it is quite plausible that the enhanced fields at the tips of projecting conductors within 1 to 2 km from a 10-MT burst at $t \lesssim 3$ ms will exceed 3 MV/m, so that some type of discharge phenomenon should be expected, it is not clear whether an upward propagating streamer will result, as in the lightning rod phenomenon. The applied field from a downward propagating cloud-to-ground stroke is rapidly increasing in time, while that from an EMP environment is nearly constant. It is also known from laboratory experiments (Ref. 22) that steady fields only slightly above breakdown over small volumes near the tip of a positive electrode generally tend to produce intermittent coronas rather than leader channels, with the corona-to-leader transition being inhibited by space charge fields which oppose the applied field in the region between the space charge and the electrode. In the lightning rod phenomenon, such space charge fields are probably overcome by the continual increase in applied field as the downward propagating stroke approaches the earth. However, in the nuclear environment the space

charges may be reduced by conduction currents through the surrounding ionized air, a possibility to which we will shortly return.

Before addressing the potential impact of ionization and air conductivity, there is another source of potentially relevant information which should be mentioned. Data obtained from laboratory studies of the breakdown of long (up to 28 m) positive-point-to-plane gaps in air (Ref. 22) have led to the adoption of empirical rules of the form $V_B(kV) \simeq 500\ d^{0.5}$ for the voltage needed to break down a gap of length d(m). Taking $d \simeq 600$ m, about the length of the longest arcs in the Mike shot, one obtains $V_B \simeq 12$ MV, whereas the present EMP calculations give a potential difference of about 10 MV (with a ± 50 percent uncertainty) over this path.

Finally, we should consider the potential effect of ionization and air conductivity. As mentioned previously, a leader channel from a positive point electrode is typically preceded by an "impulse corona" which creates a positive space charge. The effect of this space charge is to suppress further electron avalanching until (Ref. 23) the energy deposited at its stem by the electron avalanche process can be thermalized to bring the gas to a temperature of $\sim 3000°K$; at this point, thermal detachment of electrons previously attached to oxygen molecules raises the corona stem conductivity to the point where the space charges can begin to relax and also allows thermal expansion of the gas, which increases the E/N ratio allowing further avalanche development. A leader channel then develops from the corona stem (provided that the voltage has not fallen), and this leader channel propagates away from the conducting point, preceded by a new "leader corona," which feeds current into

the advancing leader channel. Depending on the applied voltage, the voltage drop along the leader, and the space charge fields of the corona, the leader may progress to bridge the entire gap, or it may eventually stop in midair.

According to this picture of discharge development, the first hurdle to overcome in creating a leader channel is to relax the space charge fields from the impulse corona. In the nuclear environment there is a new mechanism for achieving this. Since the air conductivity at relevant times and ranges is of the order of 3×10^{-5} mho/m, the space charge should be relaxed by conduction currents in times of the order of a few times $\varepsilon_o/\sigma \simeq 0.3$ μs. Thus, one would expect leader channel initiation to be very different and possibly easier in the nuclear environment than in un-ionized air.

Similar considerations should apply to leader propagation. The leader corona from a 350-kV point (i.e., E_o h $\simeq$ 35 kV/m x 10 m) would normally have (Ref. 22) a charge of several μC, which would thus draw a conduction current of about 10 A in 3×10^{-5} mho/m ionized air. This is typical of measured leader channel currents in long gaps (Refs. 22,23,24). Leader channel velocities are typically observed to be related to current by the empirical rule (Ref. 22) v (m/s) $\simeq 2 \times 10^4$ i (A). Thus a 10-A current implies a velocity of 2×10^5 m/s, which is consistent with the observed leader velocities on the Mike shot (Ref. 15). Finally, the potential drop along a leader channel for a long spark is generally observed (Ref. 22) to be of the order of E_ℓ (kV/m) $\simeq 100\ i^{-1/2}$, or about 30 kV/m for a 10-A current. Since the EMP fields are calculated (with $\pm$ 50 percent

uncertainty in J_o/σ_o) to be of this same order of magnitude at the earth's surface but will decrease with increasing elevation, it would not be surprising for the Mike lightning strokes to stop in midair, which is what may have been observed for four out of the five strokes. It should also be mentioned that there are indications (Ref. 22) in favor of even lower potential gradients in very long leader channels. This is supported both by the fact that cloud-to-ground lightning strokes commonly propagate into regions where $E_o < 20$ kV/m [these are also convergent field geometries which are harder to break down, at least in short gaps, than the divergent field geometries being discussed here (Refs. 19,22)], and by the extrapolation of data on long positive-point-to-plane gaps (mentioned earlier), which implies that a 1-m increase in gap length at $d \simeq 600$ m only increases the breakdown potential by 10 kV.

Thus, to summarize the discussion of field strength criteria for nuclear lightning initiation and propagation, it must be concluded that available data from naturally occurring ground-to-cloud lightning, from lightning rod phenomena, and from breakdown of long gaps in air cannot be unambiguously applied to predict the fields needed for creation of upward propagating lightning in an EMP environment. However, these data clearly do not rule out the possibility that the observed Mike lightning might be consistent with the type of EMP theory presented in this report. Moreover, consideration of the possible effects of ionized air conductivity on the discharge process suggests that lightning discharges might be very different and perhaps also easier to initiate and to propagate in an EMP source region than in un-ionized air.

With regard to the issue of lightning stroke curvature, it is not immediately clear whether the dominant electric field guiding the direction of stroke propagation will be the ambient

EMP field or the field due to the stroke itself. However, since one might expect any "self-field" to favor essentially vertical propagation (whereas the strokes are actually curved inward, roughly concentric about the burst point), we will assume that the strokes are tending primarily to follow the local direction of the ambient EMP field; we may then ask whether this indicated direction is consistent with EMP theory.

The predominant indication from the observed curvature is that $E_\theta >> E_r$ throughout most of the temporal and spatial range of interest. Apparently based upon Longmire's approximate analysis of Model 2 (ion-dominated conductivity, also see Figure 3), it has been suggested (Ref. 8) that this observation implies a negligible electron conductivity. Since at the expected source strength for a 10-MT burst ($S_o \simeq 3.6 \times 10^{29}$ - 1.1×10^{30} ion-pairs/m/s for $t \simeq 1$-3 ms), electronic contributions would normally be expected to dominate out to $r \simeq 800$ m to 1000 m, it has been concluded that the lightning stroke curvature demonstrates the need for some anomalous mechanisms for electron removal.

However, our present solutions for Model 3 (see Figure 4), with predominantly electronic conductivity at closer ranges and predominantly ionic conductivity farther out, clearly demonstrate that one can still find regions where $E_\theta >> E_r$ even when the electronic conductivity is not negligible throughout the region of interest. In Figure 7 we have shown the angular dependence of E_θ and E_r at $r = 960$ m and $r = 1280$ m as predicted by Model 3. It may be seen that even as close in as $r = 960$ m, E_θ clearly dominates over E_r up to elevations of 30° or more above the ground plane.

The electric field structure reflected in Figure 7 shows somewhat less inward curvature than is seen in the photographs of the Mike lightning, primarily over the upper half of the more close-in observed strokes. Thus, the ratio of ionic to

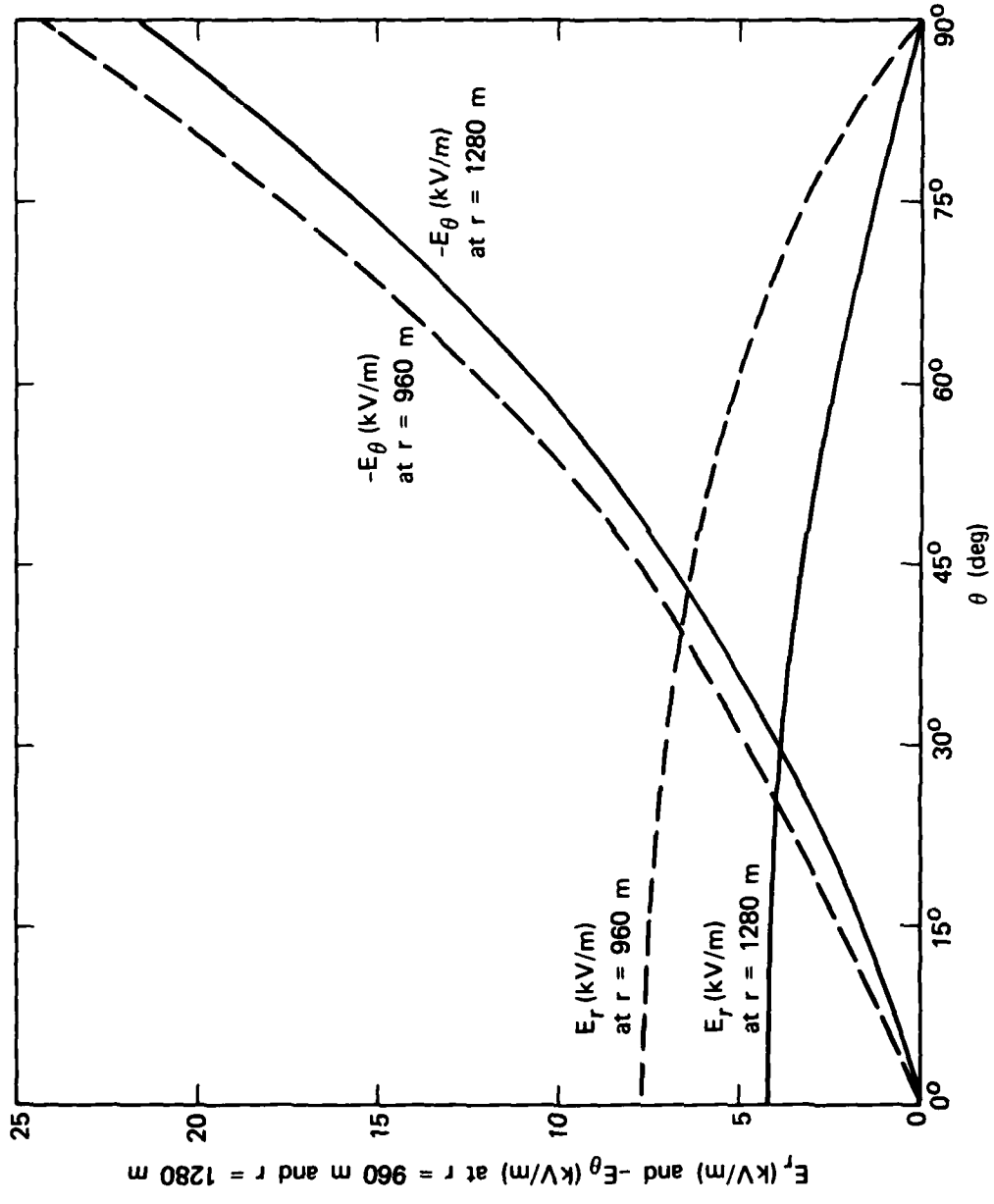

Figure 7. Results from Model 3 for E_r (kV/m) and $-E_\theta$ (kV/m) at r = 960 m and r = 1280 m (assumes λ = 320 m, $-J_o/\sigma_o$ = 63 kV/m).

electronic conductivity during the later stages of the stroke propagation was probably somewhat greater than allowed in Model 3, and the ion-dominated Model 2 may also have become applicable somewhat earlier than we have assumed. However, for the reasons given below, these observations are not inconsistent with the present theory.

First, it should be noted that the ionization rate would have fallen by about a factor of 3 over the $t \simeq 1$- to 10-ms time frame during which the lightning strokes evolved, thereby increasing the ratio σ_I/σ_e. Furthermore, it must be realized that the parameter values used in the above calculations have simply reflected our best a priori estimates. They are also subject to appreciable uncertainty. We have already mentioned the estimated ±30 to 50 percent uncertainties (at a given water vapor content and electric field strength) in the values of electron attachment rate, electron and ion mobilities, and ion-ion recombination rate constant. In addition, the value of σ_I/σ_e depends on the dose rate (which is probably not known at any given time to within a factor of 2) and the water vapor concentration (which is probably also uncertain by ±30 to 50 percent).

When accounting for these uncertainties in the parameters which influence the value of σ_I/σ_e and for the decline in dose rate throughout the $t \simeq 1$- to 10-ns time frame, the details of the observed lightning stroke curvature do not appear to be inconsistent with the existing theory of source region EMP air chemistry as reflected in the present calculations. At this time, no anomalous electron-attachment mechanisms appear to be required to rationalize the observed curvature.

REFERENCES

1. Uman, M. A., et al., J. Geophys. Res., Vol. 27, No. 9, 1972, pp. 1571-1596.

2. Longmire, C. L., "Close-In E. M. Effects Lecture VIII," Los Alamos Scientific Laboratories, LAMS-3073, 1964 (unpublished).

3. Hill, R. D., J. Geophys. Res., Vol. 78, No. 27, 1973, pp. 6355-6358.

4. Wyatt, W. T., An Improved Model for EMP-Induced Lightning, Harry Diamond Laboratories, HDL-TR-1919, 1980.

5. Longmire, C. L., IEEE Trans. Ant. and Propagat., Vol. AP-26, No. 1, 13 March 1978.

6. Longmire, C. L., and Price, H. J., EMP Simulation Concepts for MX II, Mission Research Corporation, MRC-R-368, January 1978.

7. Scheibe, M., The Increased Attachment Due to Ionization-Induced Smog in EMP Environments, Mission Research Corporation, MRC-R-532, 1979.

8. Scheibe, M., and Longmire, C. L., The Effects of Ionization-Induced Smog on EMP Environments, Mission Research Corporation, MRC-R-362, 1979.

9. Sargis, D. A., et al., Late Time Sources for Close-in EMP, Defense Nuclear Agency, DNA 3064F, 1972.

10. Cohen, M. O., et al., Time-Dependent Energy Deposition and Compton Electron Currents from Three Selected Low-Altitude Bursts, Harry Diamond Laboratories. HDL-CR-76-029-1, 1976.

11. Grover, M. K., and Gilmore, F. R., A Review of Data for Electron Mobility, Energy, and Attachment Relevant to EMP Air Chemistry, R & D Associates, RDA-TR-110002-001, 1980.

12. Jackson, J. D., Classical Electrodynamics, John Wiley & Sons, Inc., New York, 1966.

13. Gradshetyn, I., and Rhyzhik, I., Table of Integrals, Series and Products, Academic Press, New York, 1965.

REFERENCES (CONTINUED)

14. Abramowitz, M., and Stegun, E. A. (eds.), Handbook of Mathematical Functions, Dover Publications, New York, 1968.

15. Bortner, H. M., and Baurer, T. (eds.), Defense Nuclear Agency Reaction Rate Handbook, GE/TEMPO, Santa Barbara, California, revised 1977.

16. Brode, H. L., "Review of Nuclear Weapons Effects," Annual Review of Nuclear Science, Vol. 18, 1967, pp. 153-202.

17. Glasstone, S., and Dolon, P. J., (eds.), The Effects of Nuclear Weapons, 3rd Edition, U.S. DOD and USAEC, 1977, page 365.

18. Pierce, E. T., "Triggered Lightning and Some Unsuspected Lightning Hazards," AAAS 138th Annual Meeting, 1971.

19. Golde, R. H., Lightning, Vols. 1 and 2, Academic Press, New York, 1977.

20. Anderson, R. B., Ericksson, A. J., Krooninger, H., Inst. Elect. Eng., 1976, pp. 264-267.

21. Morse, P. M., and Feshback, H., Methods of Theoretical Physics, Vol. 2, McGraw-Hill Book Company, Inc., New York, 1953.

22. Water, R. T., "Spark Breakdown in Non-Uniform Fields," in Electrical Breakdown of Gases, J. M. Meek and J. D. Craggs (eds.), John Wiley & Sons, Inc., New York, 1978.

23. Gallimberti, I., "The Characteristics of the Leader Channel in Long Sparks," Paper 22, Section 2, World Electrotechnical Congress, Moscow, 1977.

24. The Les Renardieres Group, "Positive Discharges in Long Air Gaps," International Conference on High-Voltage Electrical Systems, Paris, 1977.

APPENDIX A. NUMERICAL ANALYSIS

Although we have exact closed-form solutions for each model, some numerical work is needed to obtain explicit results. Fortunately, this is not too difficult, and all of the results in this report have been obtained using a Hewlett-Packard 65 programmable calculator. The coefficients A_ℓ can be calculated directly from Eq. (10), and the Legendre polynomials and their derivatives can be easily calculated from their standard recursion relations (Refs. 13,14), starting from $P_0(\cos\theta) = 1$ and $P_1(\cos\theta) = \cos\theta$. The special functions can be calculated from their series expansions (Refs. 10,11)

$$I_{\ell+1/2}(x) = \sqrt{2/\pi}\,\frac{x^{\ell-1/2}}{(2\ell+1)!!}\sum_{k=0}^{\infty}\frac{(x^2/2)^k}{k!\;C_{k,\ell}}$$

$$C_{o,\ell} = 1;\; C_{k,\ell} = (2\ell+2k+1)C_{k-1,\ell} \qquad (k>0) \tag{A1}$$

$$K_{\ell+1/2}(x) = \sqrt{\pi/2x}\;e^{-x}\sum_{k=0}^{\ell}\frac{(\ell+k)!}{k!\,(\ell-k)!}\,(2x)^{-k} \tag{A2}$$

$$M(a,b,x) = \sum_{n=0}^{\infty}\frac{(a)_n}{(b)_n}\frac{x^n}{n!}\;;\;(a)_n = \frac{\Gamma(a+n)}{\Gamma(a)}\quad . \tag{A3}$$

The function U(a,b,x) can be expressed (Ref. 14) in terms of M(a,b,x) and M(1+a-b,2-b,x), which may then be evaluated from Eq. (A3). The gamma function may be very accurately calculated for $|x| \lesssim 1$ from a 26-term polynomial approximation (Ref. 11) for $1/\Gamma(x)$, together with the standard recursion

relation for $|x| > 1$. Considerable accuracy is sometimes needed for $\Gamma(x)$ in order to evaluate the first integral in Eq. (18).

The various integrals can be evaluated by substituting the above series expansions for the special functions and formally integrating term-by-term to obtain a series expansion for the integral. For Models 1 and 3 one has an integral of the form

$$\int_0^x dy\ I_{\ell+1/2}(y)\ \sqrt{y}\ e^{-\alpha y} = \sqrt{2/\pi}\ \left(\frac{1}{\alpha}\right)^{\ell+2}\ \frac{e^{-\alpha x}}{(2\ell+1)!!}$$

$$\times \sum_{n=0}^{\infty} \frac{(1/2\alpha^2)^n}{n!\ C_{n,\ell}}\ (2n+\ell+1)! \sum_{k=2n+\ell+2}^{\infty} \frac{(\alpha x)^k}{k!} \qquad \text{(A4)}$$

which may be evaluated by numerical summation, and

$$\int_x^{\infty} dy\ K_{\ell+1/2}(y)\sqrt{y}\ \ e^{-\alpha y} = x\ \sqrt{\pi/2} \sum_{k=0}^{\ell} \frac{(\ell+k)!}{k!\,(\ell-k)!}\ (2x)^{-k}\ E_k\left((\alpha+1)x\right) \qquad \text{(A5)}$$

which may also be numerically summed with the exponential integral $E_n(x)$ evaluated by (Ref. 14)

$$E_o(x) = \frac{1}{x}\ e^{-x}$$

$$E_1(x) = -\ .5772156649...\ -\ \ell n(x)\ -\ \sum_{m=1}^{\infty} \frac{(-x)^m}{m\ \ m!} \qquad \text{(A6)}$$

and

$$E_{m+1}(x) = \frac{1}{m}\left(e^{-x} - x\,E_m(x)\right) \quad (m \geq 1) \ .$$

For Model 2 one has integrals of the form

$$\int_x^\infty dy\ M(a,b,y)\ y^c\ e^{-2y} = \left(\frac{1}{2}\right)^{c+1} \sum_{n=0}^{\infty} \frac{(a)_n}{(b)_n} \frac{(1/2)^n}{n!}\ \gamma(n+c+1,2x) \tag{A7}$$

which may be numerically summed with the incomplete gamma function $\gamma(a,x)$ evaluated from (Ref. 14)

$$\gamma(\alpha,x) = X^\alpha \sum_{k=0}^{\infty} \frac{(-x)^k}{k!\,(k+\alpha)} \tag{A8}$$

and

$$\gamma(\alpha+1,x) = \alpha\gamma(\alpha,x) - x^\alpha e^{-x} \quad .$$

For Model 2 one also has integrals which are obtained by expressing $U(a,b,x)$ in terms of $M(a,b,x)$ and $M(1+a-b,2-b,x)$ and which are of the form

$$\int_0^x dy\ M(a,b,y) y^c e^{-2y} = \left(\frac{1}{2}\right)^{c+1}$$

$$X \sum_{n=0}^{\infty} \frac{(a)_n}{(b)_n} \left(\frac{1}{2}\right)^{n+1} \frac{1}{n!} \left(\Gamma(n+a+1) - \gamma(n+a+1,x)\right) \tag{A9}$$

which may be evaluated by numerical summation with the gamma and incomplete gamma functions evaluated as described above.

For each of the three models, $\phi_\ell(r)$ and $d\phi_\ell(r)/dr$ are calculated separately from their respective closed-form expressions. Thus, a useful cross-check of the numerical results is obtained by comparing the calculated values of $d\phi_\ell(r)/dr$ with values obtained by finite differences from the calculated values of $\phi_\ell(r)$ at nearby range points.

The numerical results for $\phi_\ell(r)$ and $d\phi_\ell(r)/dr$ are displayed in dimensionless form in Figures A1 through A6. It may be seen that in some cases the expansion in Legendre polynomials will not converge particularly rapidly, so that the accuracy with which the electric fields are calculated may sometimes be only ~10 percent. In an attempt to improve convergence with a minimum of computational effort, values for $\phi_\ell(r)$ have been estimated for the highest ℓ by extrapolation of the values for lower ℓ. In each figure, the absolute value is plotted, with the sign denoted by the (+) or (-) symbol.

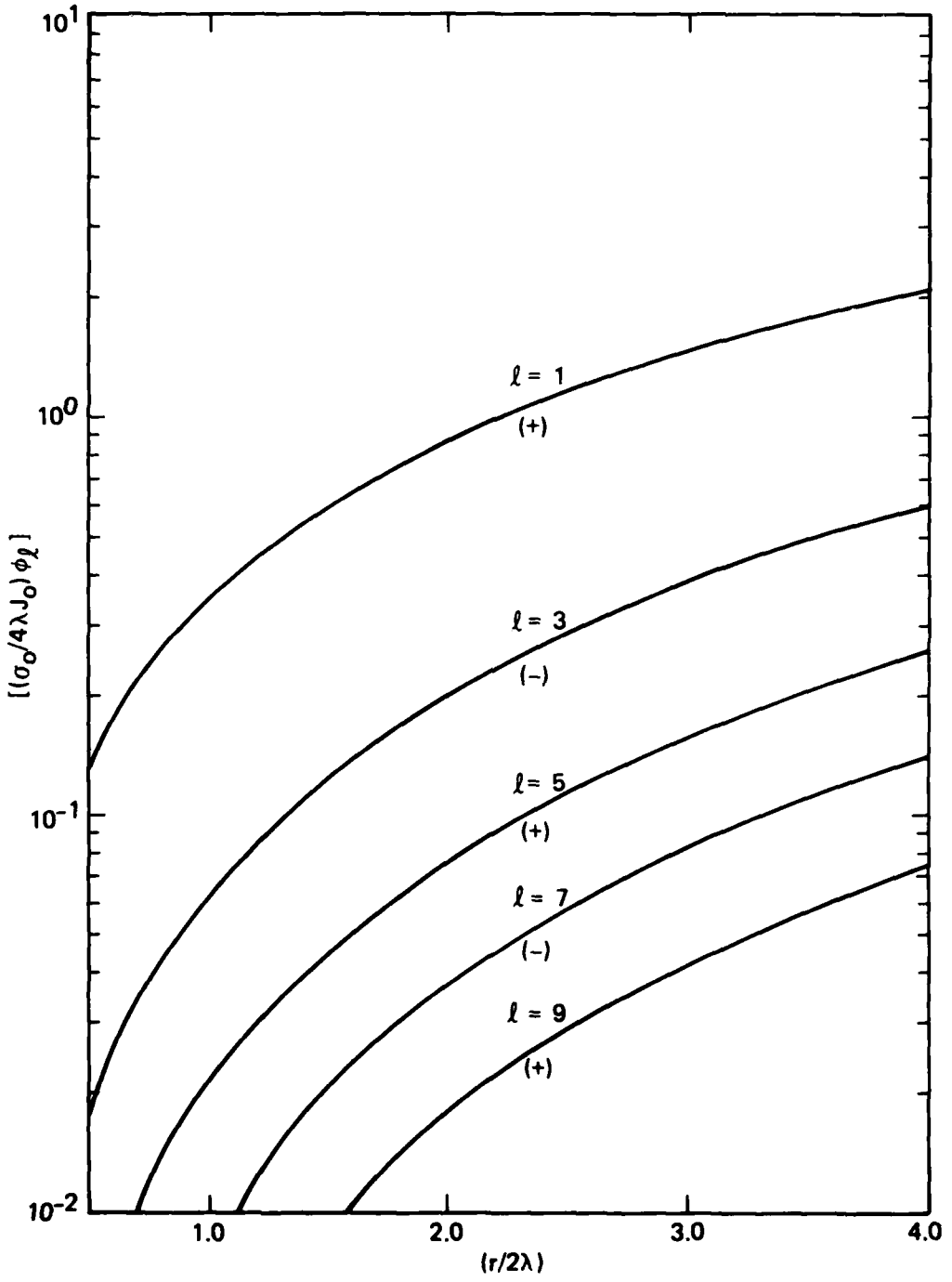

Figure A1. Dimensionless results for $\phi_\ell(r)$ from Model 1.

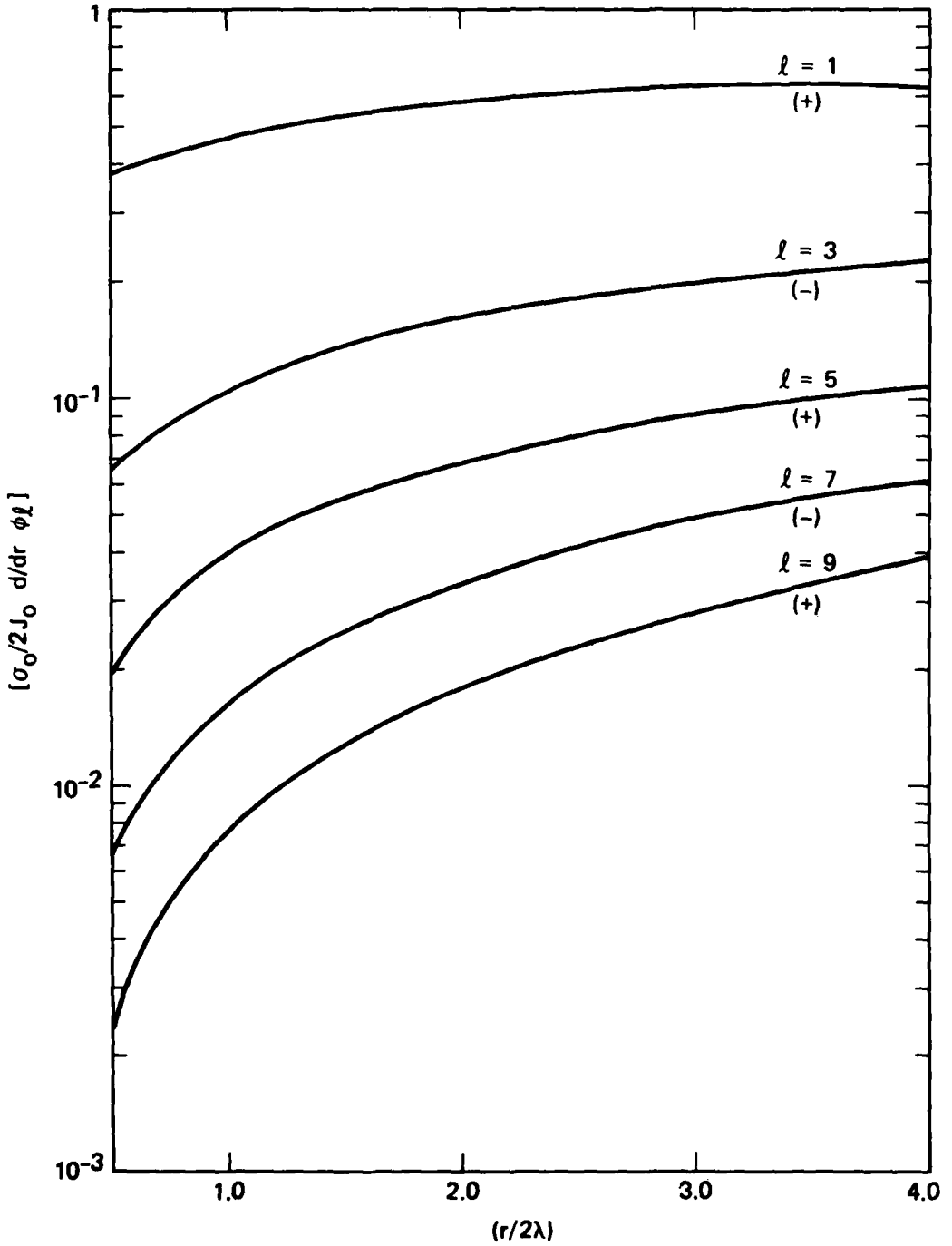

Figure A2. Dimensionless results for d/dr $\phi_\ell(r)$ for Model 1.

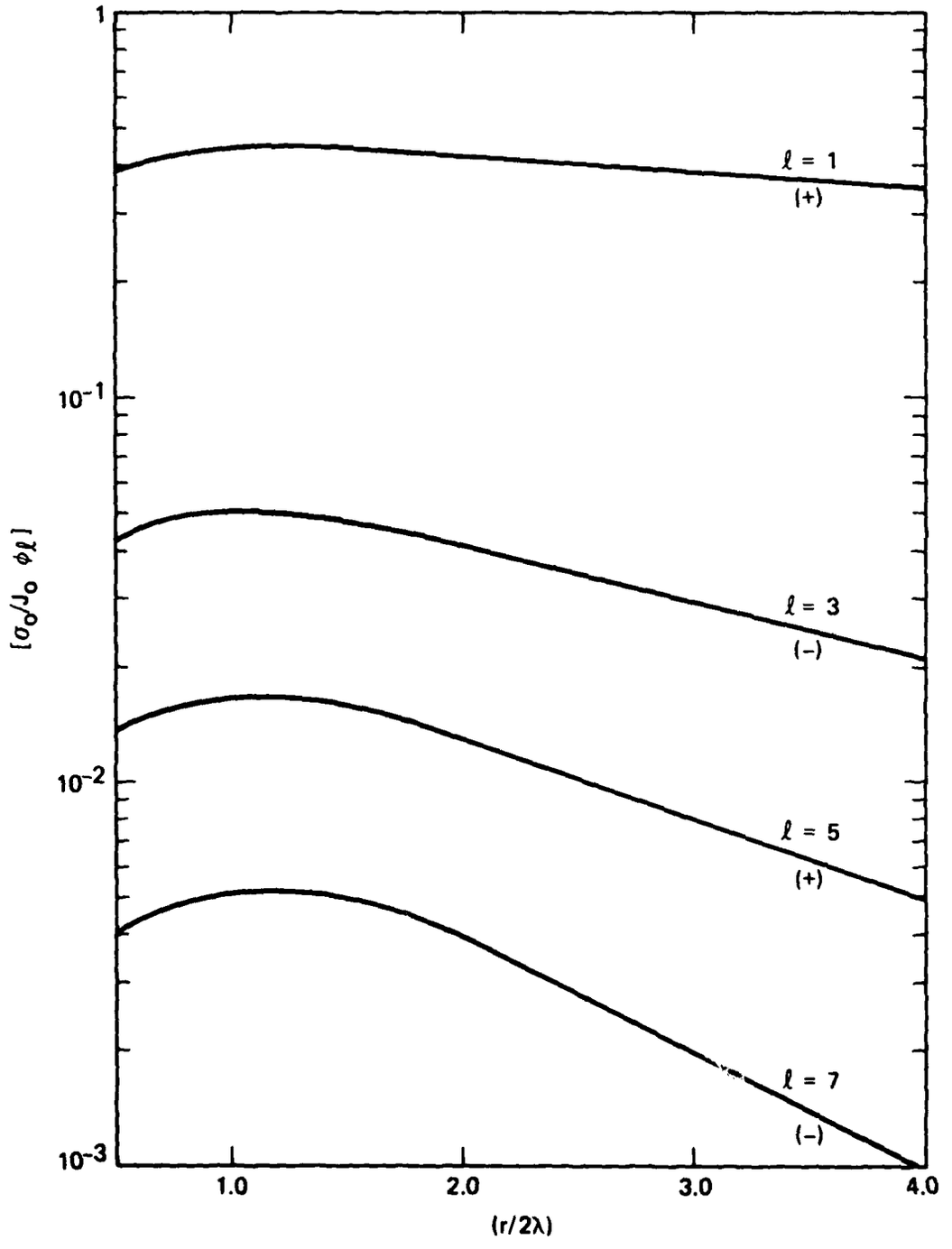

Figure A3. Dimensionless results for $\phi_\ell(r)$ from Model 2.

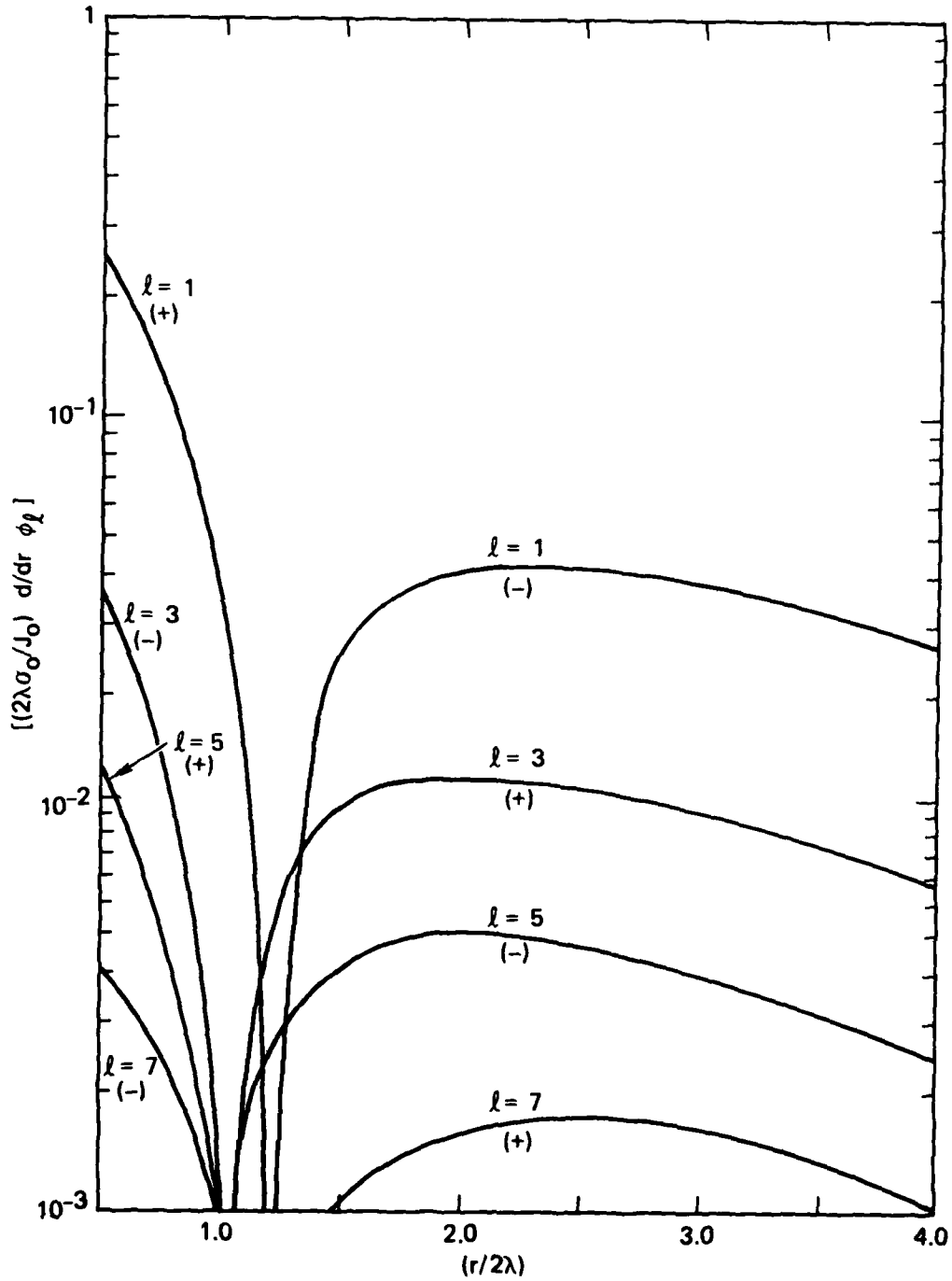

Figure A4. Dimensionless results for d/dr $\phi_\ell(r)$ from Model 2.

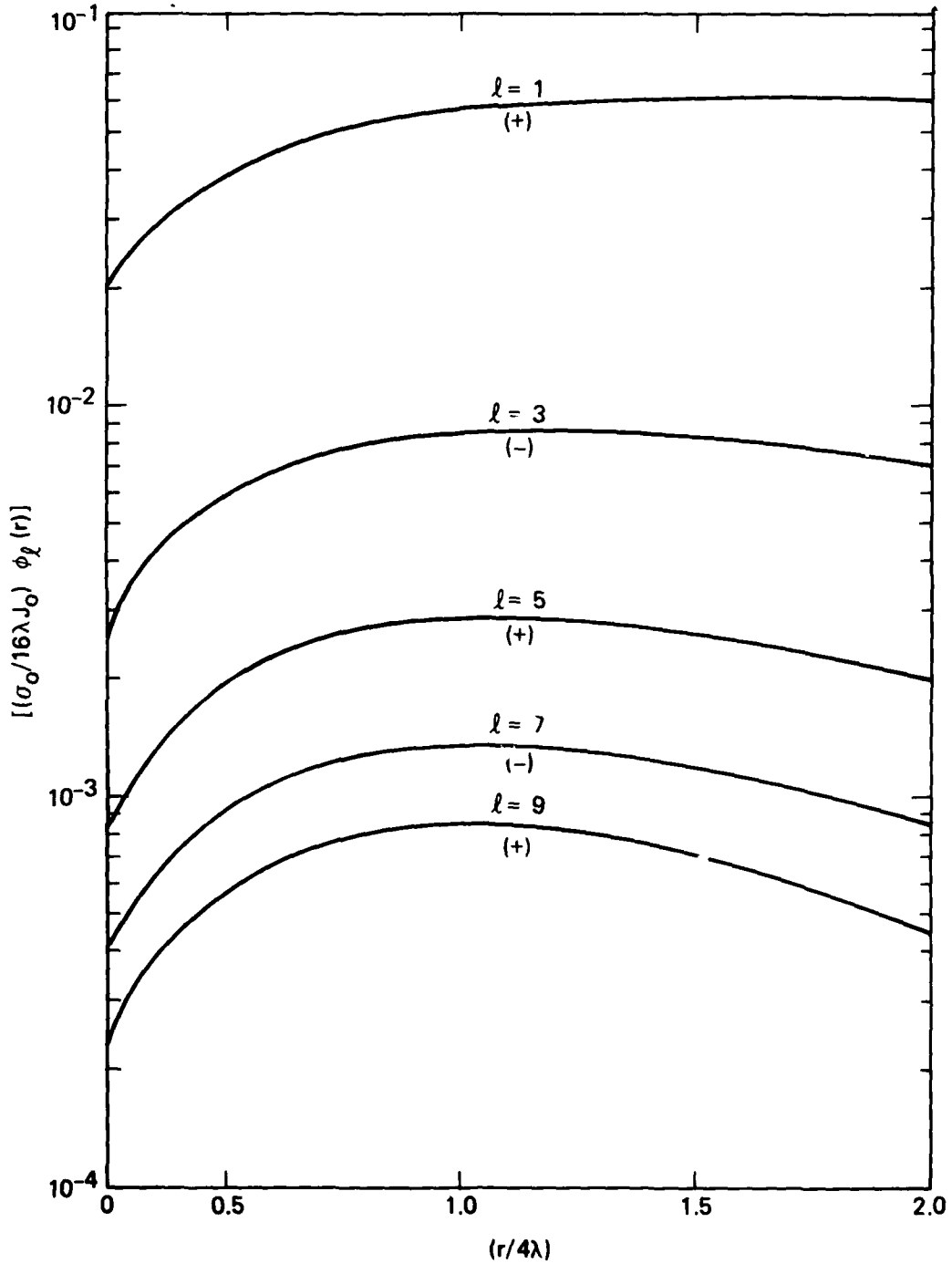

Figure A5. Dimensionless results for $\phi_\ell(r)$ for Model 3.

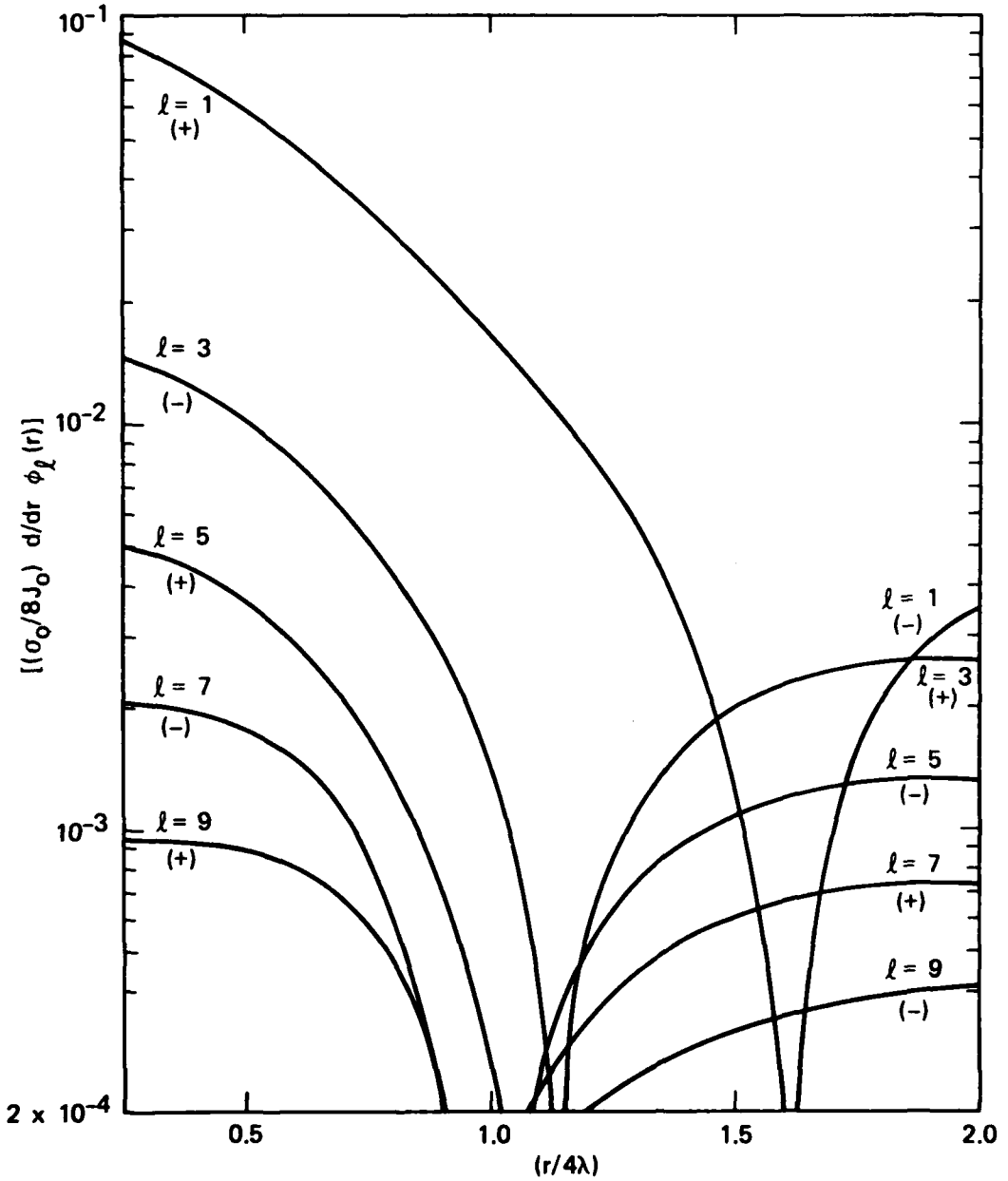

Figure A6. Dimensionless results for d/dr $\phi_\ell(r)$ for Model 3.

DISTRIBUTION LIST

DEPARTMENT OF DEFENSE

Assistant to the Secretary of Defense
Atomic Energy
ATTN: Executive Assistant

Defense Intelligence Agency
ATTN: DB-4C2, D. Spohn
ATTN: RDS-2A

Defense Nuclear Agency
ATTN: RAEV
2 cy ATTN: RAEE
4 cy ATTN: TITL

Defense Technical Info Center
12 cy ATTN: DD

Field Command
Defense Nuclear Agency
ATTN: FCTT
ATTN: FCPR, J. T. McDaniel
ATTN: FCLMC, H. R. Putnam

Field Command
Defense Nuclear Agency
Livermore Branch
ATTN: FCPRL

Under Secretary of Defense for Rsch & Engrg
ATTN: Strategic & Space Sys (OS)

DEPARTMENT OF THE ARMY

BMD Systems Command
Department of the Army
ATTN: BMDSC-HW, R. Dekalb
ATTN: BMDSC-HLE, R. Webb
ATTN: BMDSC-AOLIB

Harry Diamond Laboratories
Department of the Army
ATTN: DELHD-N-TD
ATTN: DELHD-N-TF
ATTN: DELHD-I-TL
ATTN: DELHD-N-EMC
ATTN: DELHD-N-EMA
ATTN: DELHD-N-EME
ATTN: DELHD-N-EMB
ATTN: DELHD-N-EMD
ATTN: DELHD-N-EM
ATTN: DELHD-N-RCC
ATTN: DELHD-N-RB
ATTN: NWPO
2 cy ATTN: DELHD-N-RBC

US Army Engineer Div Huntsville
ATTN: HNDED-SR

US Army Intel Threat Analysis Detachment
ATTN: Admin Officer

US Army Intelligence & Sec Cmd
ATTN: Tech Lib
ATTN: Tech Info Fac

DEPARTMENT OF THE NAVY

Naval Postgraduate School
ATTN: Code 1424, Lib

Naval Rsch Laboratory
ATTN: Code 2627, D. Folen
ATTN: Code 1434, E. Brancato
ATTN: Code 6623, R. Statler
ATTN: Code 6624

Naval Surface Weapons Center
ATTN: Code F30
ATTN: Code F32, E. Rathbun

DEPARTMENT OF THE AIR FORCE

Air University Library
Department of the Air Force
ATTN: AUL-LSE

Ballistic Missile Office
Department of the Air Force
ATTN: ENSN, J. Allen

Foreign Technology Div
Air Force Systems Command
ATTN: TQTD, B. Ballard
ATTN: NIIS, Lib

Air Force Weapons Lab
Air Force Systems Command
ATTN: NTYEE, C. Baum
ATTN: NXS
ATTN: CA
ATTN: SUL
ATTN: NTYEP, W. Page
ATTN: ELXT
ATTN: NT
ATTN: NTYE, J. Castillo
ATTN: NTN
ATTN: ELP
ATTN: NTYC, M. Schneider

Strategic Air Command
Department of the Air Force
ATTN: DEL
ATTN: NRI, G. Matzke
ATTN: XPFS, F. Tedesco
ATTN: NRI-STINFO, Lib

OTHER GOVERNMENT AGENCY

Central Intelligence Agency
ATTN: OSWR/NED

DEPARTMENT OF ENERGY CONTRACTORS

Lawrence Livermore National Lab
ATTN: L-156, H. Cabayan
ATTN: L-10, H. Kruger
ATTN: L-153, D. Meeker
ATTN: L-156, E. Miller
ATTN: L-96, T. Donich
ATTN: Tech Info Dept Lib

DEPARTMENT OF ENERGY CONTRACTORS (Continued)

Los Alamos National Lab
ATTN: MS 670, J. Hopkins
ATTN: B. Noel
ATTN: C. Benton

Sandia National Lab
ATTN: E. Hartman
ATTN: C. Vittitoe
ATTN: R. Parker

DEPARTMENT OF DEFENSE CONTRACTORS

BDM Corp
ATTN: Corporate Lib

BDM Corp
ATTN: Lib

Boeing Co
ATTN. V. Jones
ATTN: H. Wicklein
ATTN: D. Kemle
ATTN: Kent Tech Lib
ATTN: B. Hanrahan

Dikewood Corp
ATTN: C. Jones
ATTN: Tech Lib
ATTN: L. Davis

Electro-Magnetic Applications, Inc
ATTN: D. Merewether

IRT Corp
ATTN: N. Rudie
ATTN: B. Williams

JAYCOR
ATTN: E. Wenaas
ATTN: R. Stahl

JAYCOR
ATTN: W. Radasky

JAYCOR
ATTN: Lib

Kaman Sciences Corp
ATTN: N. Beauchamp
ATTN: F. Shelton
ATTN: A. Bridges

Kaman Tempo
ATTN: DASIAC
ATTN: R. Rutherford
ATTN: W. McNamara

Kaman Tempo
ATTN: DASIAC

Martin Marietta Corp
2 cy ATTN: M. Griffith

Martin Marietta Corp
ATTN: D-6074, G. Freyer

Mission Research Corp
ATTN: V. Van Lint

DEPARTMENT OF DEFENSE CONTRACTORS (Continued)

Mission Rsch Corp
ATTN: W. Crevier
ATTN: EMP Group
2 cy ATTN: C. Longmire

Mission Rsch Corp
ATTN: L. McCormick
ATTN: A. Chodorow

Mission Rsch Corp
ATTN: W. Ware
ATTN: W. Stark
ATTN: J. Lubell

McDonnell Douglas Corp
ATTN: S. Schneider

Pacific-Sierra Rsch Corp
ATTN: H. Brode
ATTN: L. Schlessinger

R & D Associates
ATTN: W. Graham
ATTN: C. Mo
ATTN: Document Control
ATTN: P. Haas
4 cy ATTN: M. Grover

R & D Associates
ATTN: J. Bombardi

Rand Corp
ATTN: W. Sollfrey
ATTN: LIB-D

Rockwell International Corp
ATTN: D/243-068, 031-CA31
ATTN: N. Rudie
ATTN: J. Monroe
ATTN: V. Michel

Rockwell International Corp
ATTN: F. Shaw

Science Applications, Inc
ATTN: R. Parkinson

Science Applications, Inc
ATTN: W. Chadsey

SRI International
ATTN: A. Whitson
ATTN: E. Vance

Sylvania Systems Group
ATTN: I. Kohlberg
ATTN: C. Thornhill
ATTN: L. Blaisdell

Sylvania Systems Group
ATTN: M. Nurefora
ATTN: J. Waldron
ATTN: A. Novenski
ATTN: D. Flood
ATTN: C. Ramsbottom
ATTN: E. Motchok

DEPARTMENT OF DEFENSE CONTRACTORS (Continued)

Teledyne Brown Engineering
ATTN: F. Leopard
ATTN: M. Price

Texas Tech University
ATTN: T. Simpson

DEPARTMENT OF DEFENSE CONTRACTORS (Continued)

TRW Defense & Space Sys Group
ATTN: O. Adams
ATTN: L. Magnolia
ATTN: R. Plebuch
ATTN: W. Gargaro
ATTN: H. Holloway


DATE
ILME